

# Beyond Plain Weave Fabrics - II. Mechanical Properties

A. Adumitroaie and E. J. Barbero<sup>1</sup>

Mechanical and Aerospace Engineering, West Virginia University,  
Morgantown, WV 26506-6106, USA

## Abstract

A new formulation for mechanical analysis of 2D biaxial orthogonal woven fabric reinforced composite materials is proposed, as required by the wide variety of fabric types offered by the textile industry. Twill and satin weaves are defined as generic families of weaving patterns based on a general 3D geometrical model of the fabric architecture presented in *Part I*. Thermoelastic material constants, progressive failure behavior, and strength are evaluated. The nonlinear stress–strain response and the strain to failure are predicted. Comparisons with available experimental data is presented. The present formulation is amenable for computer implementation in both analytical and numerical models.

## Keywords

Fabric, Composite, Plain, Twill, Satin, Weave, Stiffness, Strength.

## 1 Introduction

Woven fabrics are used as reinforcements for composite materials used in automotive, marine, aerospace, and many more applications. A large variety of fabric architectures are available besides plain weave. While most of past research has focused on plain weave fabrics, designing and engineering this class of materials requires analysis tools for dealing with the multitude of woven fabric structures now available.

A comprehensive classification of fabric reinforcements is offered in [1, 2]. The focus of the present work is on 2D biaxial orthogonal woven reinforcements, among which plain, twill, and satin weave are distinct categories. *2D* means that the woven fabric features only in-plane reinforcing properties. *Biaxial* means that tows are aligned along two directions: the fill and warp directions. *Orthogonal* means that the fill and warp tows are laid down at  $90^\circ$  with respect to each other.

The main advantages offered by textile reinforcements are: lower manufacturing costs, easier handling and processing, better forming in complicated geometrical shapes of the composite part, the possibility of applying a variety of processing techniques (e.g., hand lay-up, resin transfer molding, resin film infusion, chemical vapor infiltration), improved impact resistance and damage tolerance, reduced notch sensitivity, improved out of plane mechanical properties (e.g., as reduced delamination crack growth and improved peel strength) and the possibility of choosing among a large number of fabric architectures.

The aforementioned advantages of fabric reinforcements are accompanied by new aspects that affect the mechanical behavior of the composite material. The manufacturing process of tows interweaving results in a complex 3D internal architecture of the fabric. Even if the fabric reinforcement features 2D in-plane reinforcing properties, it has a 3D internal architecture due to the waviness induced by the weaving process. This 3D architecture results in complex strain/stress field in the composite material, triggering new failure mechanisms and failure modes not seen in traditional unidirectional laminates. For example, specific failure

---

<sup>1</sup>Corresponding author. The final publication is available at <http://dx.doi.org/10.1016/j.compstruct.2010.11.016>

mechanisms encountered in fabric reinforced composites include: intra-ply delamination (i.e., delamination between overlapping tows of the same woven ply), transverse normal and shear failure modes under axial loading, and failure of pure matrix regions. As a consequence, the internal 3D structure of the reinforcement translates in degradation of stiffness and strength properties of the composite material. For example, knock-down factors of up to 10 – 30% for stiffness and up to 15 – 23% for axial strength are reported in [1]. Similar trends can be identified from experimental observations [3–5].

Two different approaches can be used while studying the mechanical behavior of fabric reinforced composites: analytical and numerical models. Analytical models are easier to use in practical applications, facilitating parametric studies. Usually, analytical models rely on simplifying assumptions that might restrict the degree of generality of the model. Numerical models are able to better describe the interactions inside the 3D structure of the fabric composite. However, a higher modeling effort and custom numerical discretizations for individual fabric architectures are required. Most modeling approaches are based on the repetitive unit cell (RUC) technique; i.e., to analyze the smallest geometrical repetitive unit of the textile reinforced composite material. The resulting RUC properties are considered to be representative for the material.

Three analytical models are proposed in [6, 7] to evaluate the elastic properties of plain and satin weave reinforcements, namely the mosaic, crimp and bridging models. The mosaic model does not consider the undulation of fill and warp tows, it is used to predict in-plane elastic properties of the composite material only, and it does not address material strength. The crimp model (fiber undulation model) considers the tow waviness along only one direction and it is used to predict the failure initiation only, but not strength. The bridging model, which is a combination of the previous two models, is dedicated to more accurate evaluation of the material properties of satin weaves. The mosaic model is generalized in [8] in order to calculate the elastic material properties of hybrid woven fabrics, which are fabrics with different dimensions or containing different types of fibers.

Improvement of the fiber undulation model is done in [9, 10] for the case of *plain weave* only. Additional aspects of the material mechanics are considered, as the extension-bending local coupling specific to unsymmetric stacking sequences and the out of plane stress components generated by the out of plane tow waviness. However, the model in [9, 10] features the same limitations of the geometrical representation as the fiber undulation model (i.e., a 2D geometrical model considering the tow undulation along only one direction). In plane stress distribution under axial tensile loading is reported in [9] in order to perform progressive failure analysis of the composite material, by considering early failure modes generated by the complex geometry of the woven fabric. The simplified 2D geometrical model requires for the use of iso-stress assumption in order to perform stress analysis, which drastically over simplifies the stress distribution in the reinforcing structure. Although an improved 3D geometrical model (considering tow undulation in both fill and warp directions) for plain weave fabrics is proposed in [10], the model is used only for calculating material elastic constants.

Analysis of *plain weave* fabric reinforced composites is made in [11–17]. In [12, 14] an accurate 3D geometrical model considering the fiber undulation on both fill and warp directions of plain weave is presented. The material thermo-elastic properties are calculated based on either iso-strain, or combined iso-stress / iso-strain model. The analysis is performed at ply level and the whole set of in-plane thermo-elastic constants of the composite material are calculated. The model is further developed in [15–17] where failure behavior of the composite material is addressed. A very detailed 3D geometrical analysis of the plain weave reinforcement is presented in [15]. Stress calculation and progressive failure behavior are performed in [16]. Multiple failure modes that can be encountered due to the complex spatial structure of the plain weave reinforcement are accounted for. Multiple sources of non-linearity are considered: material nonlinearity due to nonlinear constitutive behavior of the matrix constituent, material nonlinearity due to progressive failure and stiffness reduction, and geometrical nonlinearity due to straightening of the wavy tows under tensile loading. The analysis is performed in an incremental, iterative manner. A special geometrical model is generated for stress calculation, and stresses are evaluated based on the method of cells and combination of iso-stress and iso-strain assumptions. A beam on elastic foundation model is used in order to simulate the tow behavior after matrix failure initiation, when the bridging effect between adjacent tows (i.e., the capacity of adjacent tows to transmit loads from each other, due to the matrix connection between them) is progressively lost. All these modeling features are expected to confer a high level of accuracy, but at the same time they confine the applicability of the model to *plain weave* only under *uniaxial loading* only. The

effect of tow width, tow thickness, and inter-tows gap is analyzed in [17].

A higher level of generality for the reinforcing architecture is sought in [18, 19], where the case of two *particular* types of satin weaves (5- and 8-harness satin) and two cases of braided fabrics are analyzed based on 3D geometrical description. The elastic properties are modeled in [18] based on iso-strain assumption over RUC. The stress and failure analysis are performed in [19] based on iso-strain assumption over RUC. However, only the classical *plain weave* case and one case of braided fabric are analyzed in [19]. Nonlinearities are considered in the form of nonlinear matrix behavior, nonlinearity due to progressive failure and stiffness reduction, and geometrical nonlinearity due to tow reorientation under axial loading.

3D geometrical models of *particular* cases of twill and satin weave are presented in [20, 21]. Elastic material properties are calculated based on iso-strain assumption in [20] and stress analysis is carried out based on iso-stress assumption in [21]. The model is able to identify failure initiation in different components (fill, warp, matrix) of the composite, allowing for the application of a stiffness reduction scheme. However, individual failure modes in the same tow are not identified because the failure analysis is based on quadratic failure criteria, which does not allow to clearly state if failure in the main load carrying tows is secondary (matrix dominated), or primary (fiber dominated). Hybridization is considered in the description of the woven fabric architecture in [20, 21].

The same approach of calculating stresses based on a iso-stress assumption over RUC is applied in [22] for *plain weave* case. Only the failure initiation is predicted. Stiffness properties are evaluated based on either iso-stress, iso-strain, or combinations of the first two, obtaining in this way lower and upper bounds of stiffness, as well as intermediate values.

The *plain weave* and *particular* cases of 5- and 8-harness satin weaves (5/3/1 and 8/3/1 in the nomenclature of the present paper) are treated in [23], where only elastic analysis is performed. Local bending-extension coupling terms of classical laminate theory (CLT) are included.

An attempt of analyzing families of weaving styles rather than building individual models for individual weaves is made in [24, 25]. The RUC is discretized in elements, and composite material properties are calculated by assembling the properties of individual elements, based on either iso-stress or iso-strain assumptions. Iso-stress or iso-strain models over RUC are used to calculate local stresses at fiber and matrix constituents level, using the *bridging* micro-mechanics model [26]. The strength analysis is carried out at the level of fiber and matrix constituents. Local stresses in individual fiber/matrix components are averaged over different locations of the same tow, and between different orthogonal tows, and the resulting averaged value for fiber/matrix stress is casted in a maximum stress failure criteria. This procedure of failure analysis does not identify any mode of early damage in the fabric structure, and the averaging procedure is not justified. The elastic analysis is carried up for plain weave and one particular case of each 5-harness and 8-harness weaves, as well as two types of braids. Strength analysis is performed for braids only.

A systematic approach to model woven fabric reinforcements in a generalized manner is attempted in [27]. However, only elastic properties are calculated, based on either iso-stress or iso-strain assumptions at RUC level.

The second method of analyzing mechanical properties of fabric reinforced composites is through finite element analysis (FEA) [28]. While more accurate, the FEA method is difficult to use for parametric studies, unless automatic parametric mesh generation based on automatic geometrical model generation is implemented.

In [29] the FEA method is used to predict the elastic material properties, but the approach is not suitable for stress and failure analysis. The volume of calculations is reduced by considering the RUC discretization with only one element through the thickness, as opposed to 3D discretization of each fill, warp and pure matrix constituents in other FEA models. The individual elastic properties of each element are assigned based on effective properties of the fill-warp-matrix stacking sequence and orientation at the element location, which are calculated based on combined in-plane iso-strain and out-plane iso-stress hypothesis. 3D overall elastic properties of RUC are calculated by solving the FE model with periodic boundary conditions. The simplified technique of only one element through the thickness can be afforded because only the elastic problem is addressed.

Failure analysis by FEA method is more involved [30–32]. The problem of *plain weave* is treated in [30], where incremental-iterative analysis for the tensile and shear loading cases are performed. Nonlinear effects generated by the matrix constitutive behavior and the local stiffness reduction (at individual Gauss points of each FE) due to progressive failure inside of the reinforcing structure is considered. Early modes of failure are

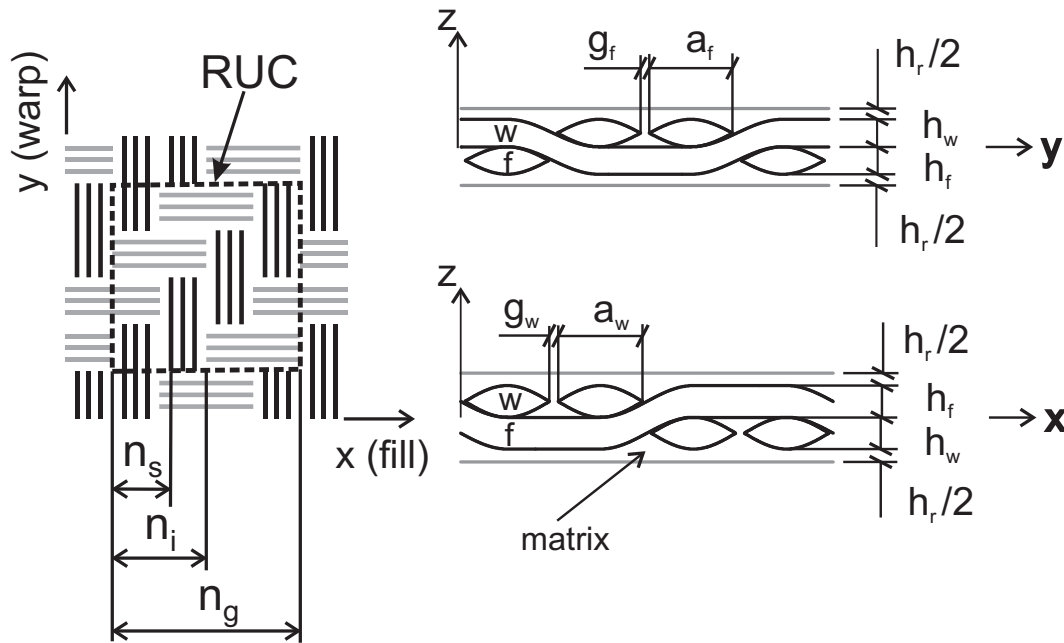


Figure 1: Geometrical parameters of the woven reinforcement. A 4/1/2 twill is depicted. Subscripts denote: f=fill, w=warp, r=resin.

identified and monitored, individual stiffness reduction coefficients are assigned to individual failure modes, and stress-strain curves up to final failure are recorded. The same method is considered in [31], where the geometric nonlinearity is also considered in the incremental-iterative procedure. Different weaving patterns (plain weave and *particular* cases of 4-, 5-, 8-satin, and twill) are analyzed. The influence of the weaving style on the failure behavior and strength properties of the composite material is for the first time assessed in an analysis of woven fabric composites. Due to the large number of elements required for a fine mesh of the RUC, reduced representative portions of the RUC are selected for the FEA analysis, based on accordingly modified periodic boundary condition imposed to the model.

Due to the inability of existing methods to predict strength of broad families of 2D fabric reinforced composites, a new approach is needed. Therefore, the objective of the present paper is the evaluation of the mechanical properties of families of 2D biaxial orthogonal woven fabric reinforced composites in an automated general way. In-plane thermo-elastic material constants are calculated. Progressive failure behavior is modeled. Individual modes of failure in fill/warp/matrix constituents are monitored while applying an incremental, iterative loading procedure. A stiffness reduction scheme is proposed in order to account for the effect of progressive damage on the stress-strain behavior of the composite material up to failure under uniaxial tensile and shear loading. The geometric model described in *Part I* [33] for families of twill/satin woven fabric reinforcements is used as starting point.

The reinforcing configuration includes the geometrical parameters of tows and the parameters describing the weaving pattern. Detailed analysis of the influence on strength of the reinforcing configuration is performed. The parameters having a major influence are identified, and methods for improving the material properties of the composites are concluded from the results. Comparison between the present woven fabric (WF) model and simplified methods of strength evaluation is performed. Comparison between the analytically predicted stress-strain behavior up to final failure and experimental results is presented for both uni-axial tensile and shear loading.

The ability of the proposed model for parametric studies based on varying both the reinforcing weaving style and the geometrical parameters of individual weaving styles are considered to be of interest for the design and analysis of woven fabric reinforced composite materials.

## 2 Material Properties of Woven Fabric composites

A model to predict mechanical properties, i.e., hygro-thermo-elastic constants and progressive failure behavior and strength of 2D biaxial orthogonal woven fabric (WF) reinforced composite material is proposed in this section. The model is based on the analysis of a representative unit cell (RUC). The geometrical parameters of the reinforcement, which are required as input data, are (Fig. 1):

- The fill (f) and warp (w) tow width  $a_f, a_w$ , tow thickness  $h_f, h_w$ , and gap between two adjacent tows  $g_f, g_w$ .
- The harness  $n_g$ , which is the number of tows in the repetitive unit cell (four in Fig. 1)
- The shift  $n_s$  between interlacing regions of two consecutive fill tows (one in Fig. 1) and
- The interlacing  $n_i$ , which is number of warp tows *over* a fill tow, in the interlacing region (two in Fig. 1.)

Additional geometrical quantities are calculated based on the aforementioned input parameters, as shown in *Part I* [33]:

- The fill/warp local undulation angles  $\theta_f(x, y), \theta_w(x, y)$
- The length of a fill/warp tow inside RUC  $L_f, L_w$
- The fill/warp cross-sectional areas  $A_f, A_w$
- The volume of a fill/warp tow inside RUC  $v_f, v_w$
- The total volume of RUC  $v_{RUC}$ , and
- The meso-scale volume fraction  $V_{meso}$  of fill and warp tows inside RUC.

Two coordinate systems (c.s.) are defined in order to analyze the properties of individual tows inside of the composite:

- The material c.s. 1, 2, 3 of each fill/warp tow regarded as UD composites, having the axes oriented along the local principal material directions of the tow, and
- The global c.s.  $x, y, z$  of the RUC, having the in-plane axes oriented along the fill and warp orthogonal directions.

### 2.1 Tow and RUC fiber volume fractions

Two important parameters for the evaluation of the elastic properties and strength of the fabric reinforced composite material are the *overall* fiber volume fraction inside the RUC,  $V_o^f$ , and *tow* fiber volume fraction  $V_f^f$  and  $V_w^f$ , i.e., the fiber volume fraction inside the fill and warp tows. The overall fiber volume fraction is different in value from the tow fiber volume fraction for the case of woven fabrics reinforced composites due to waviness of the tows and lenticular shape of tow cross-section, which requires pure matrix pockets to fill the space between the tows.

The governing parameters in the mechanical model are the tow fiber volume fractions  $V_f^f$  and  $V_w^f$ . Mechanical properties (elastic constants and strength values) of the tow, regarded as uni-directional (UD)

fiber reinforced composite, are evaluated based on  $V_f^f$  and  $V_w^f$  through the use of micro-mechanical models [2, chapter 4]. Tow properties are then translated into woven fabric (WF) reinforced composite properties considering the influence of three fabric reinforcement parameters: tow waviness, tow cross-sectional shape, and gap between tows. Thus, precise evaluation of the tow fiber volume fractions  $V_f^f, V_w^f$ , is a requirement for the mechanical model of the WF composite material.

Many models in the literature [6, 9, 10, 23] assign arbitrary values (0.7 – 0.85) to  $V_t^f$ , where  $t$  stands for *tow*, whether it is fill or warp. However, such approximations are not necessary. A direct way to evaluate  $V_t^f$  for WF composites is through image analysis measurement of tow cross-sectional area and total area of the fibers inside the tow cross-section. While this method might be more precise because the influence of all manufacturing parameters is included in the direct measurement procedure, it might also be tedious and requiring special equipment and techniques. In this paper, the fiber volume fraction inside the tow  $V_t^f$  is calculated in terms of available data.

If the number of fibers  $N_f$  inside a tow, the diameter of individual fibers  $d_f$ , and the cross-sectional area of the tow  $A_t$  are known quantities, then, the tow fiber volume fraction can be calculated as

$$V_t^f = N_f \frac{\pi d_f^2}{4A_t} \quad (1)$$

If the density of the fiber material  $\rho$  and the tow linear density  $\lambda_L$  defined as the mass per unit length of tow (also known as *denier* or *TEX*) are known, then the tow fiber volume fraction can be calculated as

$$V_t^f = \frac{\lambda_L}{\rho A_t} \quad (2)$$

Equations (1) and (2) have the advantage that they allow for individual evaluation of fill and warp fiber volume fractions if their linear density are different. The tow cross-sectional area  $A_t$  is found after compaction by photomicrographic observation or estimated from experience.

A direct method for evaluating the overall RUC fiber volume fraction  $V_o^f$  is through standardized burn-out or chemical dissolution methods [34, 35]. However, if these experimental methods are not at hand, indirect ways of evaluation are available [2, chapter 4].

Thus, if the tow linear density  $\lambda_L$  and fiber density  $\rho$  are known, then the overall fiber volume fraction  $V_o^f$  can be calculated as

$$V_o^f = \frac{\lambda_L}{\rho} \frac{n_g(L_f + L_w)}{v_{RUC}} \quad (3)$$

If the fabric surface density  $\lambda_S$ , defined as the mass of dry fabric per unit surface, the fiber material density  $\rho$ , and the thickness of the lamina  $h_c$  are known, then  $V_o^f$  can be calculated as

$$V_o^f = \frac{\lambda_S}{\rho h_c} \quad (4)$$

Equations (3) and (4) assume identical fill and warp tows. This assumption makes (3) and (4) not applicable for hybrid fabrics. Moreover, the possible ply nesting effect is not reflected in (3) and (4).

The volume fraction of tows inside the RUC is

$$V_{meso} = (v_f + v_w)/v_{RUC} \quad (5)$$

where  $v_f, v_w$ , are the volumes of the fill and warp tows, respectively; both computed by the model. The volume of the RUC is denoted by  $v_{RUC}$ .

Finally, a direct relationship exists between the overall and tow fiber volume fractions, as follows

$$V_t^f = V_o^f / V_{meso} \quad (6)$$

The advantage of using (6) is that the tow fiber volume fraction is calculated rather than being assumed at an arbitrary value as it is sometimes done in the literature. Accurate values can be calculated through (6), provided the geometrical model used to calculate  $V_{meso}$  is accurate. Equation (6) assumes identical fill

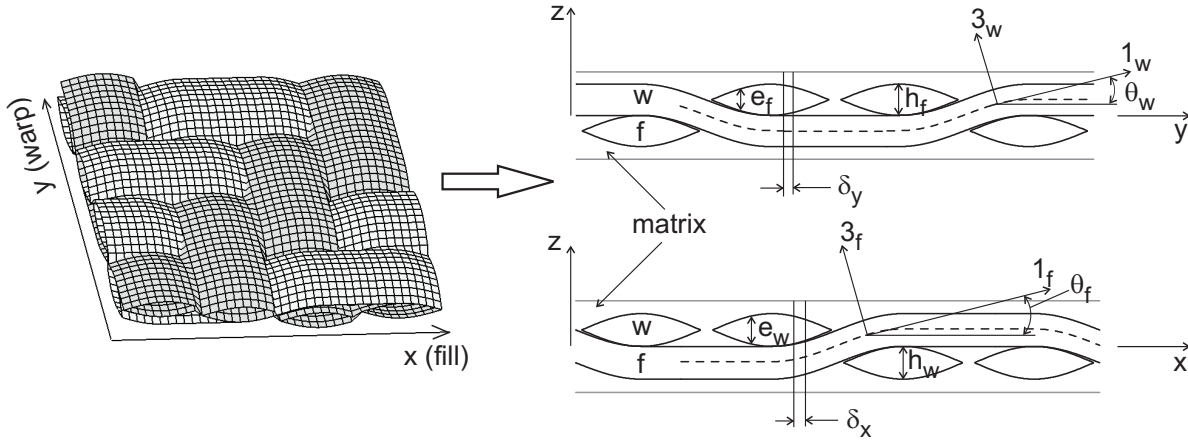


Figure 2: Fill and warp undulation for the case of 4/1/2 twill weave. See also Fig. 1

and warp tows, and no nesting effect is included. Even more accurate values of the tow fiber volume fraction  $V_t^f$  can be calculated based on (6) if the overall fiber volume fraction  $V_o^f$  is determined experimentally. Calculation of  $V_t^f$  based on this method is utilized in the present work.

An approximate method, called equivalent cross-ply (CP) method, is sometimes used in practice for estimating the properties of fabric reinforced composites [2, chapter 9]. In the (CP) method, the WF composite is approximated by a symmetric cross-ply laminate with the same total thickness as the WF composite, and having a fiber volume fraction equal to  $V_o^f$ . This method might be considered for tight WF reinforcements, with no gap between adjacent tows. However, the method is grossly inaccurate for WF with gaps. Furthermore, it has been shown in [11] that the method of equivalent cross-ply laminate provides some good results for thermo-elastic properties, but not so for strength properties.

Another approximate method, the equivalent UD lamina, is proposed in [15–17], namely approximating the WF composite as an uni-directional (UD) composite having a fiber volume fraction equal to  $V_e^f$ , where  $V_e^f$  is the effective fiber volume fraction defined as the ratio between the total cross-sectional area of the fibers inside the load carrying tow, and the total cross-sectional area of the RUC transverse to the load direction, i.e.,

$$V_e^f = V_t^f \frac{A_t}{w_t h_c} \quad (7)$$

where the quantities  $A_t$ ,  $w_t = a_t + g_t$ ,  $V_t^f$  refers to the tow that plays the role of load bearing for the case of uniaxial loading (e.g., the fill tow if the load is applied along the fill direction), and  $h_c = h_f + h_w + h_r$  is the lamina thickness (see Fig 1). This approach applies only for uniaxial tensile loading case and it is unconservative in many cases.

## 2.2 Hygro-thermo-elastic properties

Due to different undulation angle and different cross-sectional thickness of the fill, warp, and matrix constituents at different  $(x, y)$  locations in the RUC (Fig. 2), a field of hygro-thermo-elastic material properties is generated over the RUC. At each  $(x, y)$  location, classical laminate theory (CLT) is applied considering a local cross-ply stacking sequence of fill, warp, and matrix constituents. The order and the number of constituents is given by the  $(x, y)$  position inside RUC. The hygro-thermo-elastic properties of each constituent at each  $(x, y)$  location is required and CLT is then point-wise applied in order to calculate the field of composite material properties at each  $(x, y)$  location.

Based on this point-wise CLT approach, the field of composite material stiffness coefficients is calculated as

$$[A(x, y)], [B(x, y)], [D(x, y)] = \int_{-h_c/2}^{h_c/2} (1, z, z^2) \cdot [\bar{Q}(x, y)] dz \quad (8)$$

where  $\overline{Q}(x, y)$  is the reduced (in-plane) stiffness matrix of the fill, warp, and matrix constituents, transformed according with the local  $\theta_f(x, y), \theta_w(x, y)$ , undulation angles (Appendix 1, (29), and  $h_c = h_f + h_w + h_r$  is the ply thickness (see Fig. 1.))

Similarly, the field of local in-plane hygro-thermal induced loads is calculated as

$$\begin{aligned} \{N(x, y)\}^T &= \Delta T \int_{-h_c/2}^{h_c/2} [\overline{Q}(x, y)] \cdot \{\alpha(x, y)\} dz \\ \{N(x, y)\}^M &= \Delta M \int_{-h_c/2}^{h_c/2} [\overline{Q}(x, y)] \cdot \{\beta(x, y)\} dz \end{aligned} \quad (9)$$

where  $\{\alpha(x, y)\} = \{\alpha_x, \alpha_y, \alpha_{xy}\}(x, y)$ ,  $\{\beta(x, y)\} = \{\beta_x, \beta_y, \beta_{xy}\}(x, y)$  represent the reduced (in-plane) thermal and moisture linear expansion coefficients vectors of the fill, warp, and matrix constituents, transformed according with their local  $\theta_f(x, y), \theta_w(x, y)$ , undulation angles (Appendix 1, (32)). The superscripts  $T, M$  in (9) stand for *thermal* and *moisture* respectively, and  $\Delta T, \Delta M$  are the change in temperature and moisture content, respectively.

The pure matrix requires no coordinate transformation in (8) and (9) because it is isotropic. Only the thickness of the pure matrix layer at each  $(x, y)$  location has to be calculated from the geometrical model.

Additional assumptions are required in order to assemble the 2D field of mechanical properties (8) and (9). Common assumptions made in the analytical models available in the literature are based on the elastic theory of the non-homogeneous body [1]. These assumptions are made in order to homogenize (integrate) the local material properties into overall properties (8), (9). Thus, either the *iso-stress* (i.e., compliance average, also called Reuss model) or the *iso-strain* (i.e., stiffness average, also called Voigt model) assumption are used, providing lower and upper bonds for the overall properties of the composite material, respectively.

In this work, the overall in-plane stiffness coefficients are evaluated using the iso-strain assumption

$$[A] = \frac{1}{(n_g w_f)(n_g w_w)} \int_0^{n_g w_f} \int_0^{n_g w_w} [A(x, y)] dx dy \quad (10)$$

because it is shown to give better correlation with experimental data [12, 24].

The overall in-plane thermal and moisture loads are evaluated using a combined iso-stress and iso-strain assumption

$$\{N\}^{T, M} = \frac{1}{(n_g w_f)(n_g w_w)} \int_0^{n_g w_f} \int_0^{n_g w_w} \{N^{T, M}(x, y)\} dx dy \quad (11)$$

because it is the best model for thermal/moisture loads, as shown in [12, 24]. In (10), (11),  $[A(x, y)]$  is provided by (8),  $\{N\}^{T, M} = \{N_x, N_y, N_{xy}\}^{T, M}$  is provided by (9),  $w_f = a_f + g_f$ , and  $w_w = a_w + g_w$ . The later is simply the width of the tow plus the gap. Therefore, the integration is carried out over the length and width of the RUC, i.e., over the pitch of the fabric,  $p_f = n_g w_f$  and  $p_w = n_g w_w$ .

The in-plane engineering elastic constants are calculated as

$$\begin{aligned} E_x &= (\alpha_{11} h_c)^{-1} \\ E_y &= (\alpha_{22} h_c)^{-1} \\ G_{xy} &= (\alpha_{66} h_c)^{-1} \\ \nu_{xy} &= -\frac{\alpha_{12}}{\alpha_{11}} \end{aligned} \quad (12)$$

and the in-plane thermal and moisture expansion coefficients vectors  $\{\alpha\} = \{\alpha_x, \alpha_y, \alpha_{xy}\}$  and  $\{\beta\} = \{\beta_x, \beta_y, \beta_{xy}\}$  are calculated as

$$\begin{aligned} \{\alpha\} &= \frac{1}{\Delta T} [A]^{-1} \{N\}^T \\ \{\beta\} &= \frac{1}{\Delta M} [A]^{-1} \{N\}^M \end{aligned} \quad (13)$$

A similar averaging procedure can be applied for flexural components of stiffness coefficients and moisture/thermal expansion coefficients, if required.

### 2.3 Strength properties

In this work, stress analysis, progressive failure, and strength evaluation are performed using an incremental–iterative procedure and the maximum stress failure criterion. The procedure was proposed in [11] for the case of plain weave, and it is extended here for the general case of twill/satin weave reinforcements. Modifications are made to the progressive failure model in [11] regarding the stiffness reduction procedure, in order to achieve better agreement with experimental data for both stress and strain to failure.

2D discretization of the RUC (similar to FEA meshing, see Fig. 2) along both  $x$  and  $y$  directions is done in order to perform the progressive failure and strength analysis. The discretization procedure results in a number of elements with in-plane dimensions  $\delta x \times \delta y$ , having a through-thickness stacking sequence of matrix–fill–warp–matrix constituents, with the order of the constituents given by the  $(x, y)$  location of the center of each element. Also, the number of the constituents in each element is function of the position  $(x, y)$ . The constituents may be matrix–fill–warp–matrix for an element situated at a cross-over region of fill and warp, matrix–warp–matrix or matrix–fill–matrix for an element situated inside of the gap region between two adjacent fill/warp tows, or only matrix for the whole thickness of the element for the matrix pockets at the intersection between two consecutive fill tows with two consecutive warp tows, in the case of WF with gaps between adjacent tows.

The progressive failure analysis is based on an element stiffness reduction procedure. For this, stresses in each fill–warp–matrix constituent (at position  $z$ ) in each element are calculated at the  $x, y$ , center of each element. The mesh is refined until the computed strength value converges within a prescribed tolerance (5% tolerance for mesh convergence and  $5 \text{ N/mm}^2$  load step are used in this study). An automatic meshing procedure has been implemented in order to perform the meshing operation for any weaving pattern.

The first assumption in the stress analysis is to consider the RUC as being bending restrained. This assumption implies that the local extension–bending coupling due to the unsymmetric nature of the stacking sequence at any RUC location is restrained by the constraining effect of the neighboring plies. Thus, the simplified expression (14) of the local constitutive equation of the material is used, without involving the flexural stiffness matrices  $[B(x, y)], [D(x, y)]$  from (8). The bending restrained assumption is more accurate as the number of WF reinforced plies increases. Models based on CLT and bending restrained assumption can be found in [20–22]. The assumption is also implicitly involved in the 3D stiffness models in [24, 27, 29, 36], where despite additional information regarding the out of plane elastic constants, the plate behavior of the WF reinforced composite material (i.e., extension–bending coupling) is actually neglected. Models based on CLT taking into account the effect of local bending deformation are presented in [9, 10, 23].

The second assumption in the stress analysis is the iso–stress load distribution from RUC level to element level. The load distribution problem is difficult to be set to a high level of precision in an analytical model, especially when a high level of weave pattern generality is sought as in the case of the present model. The iso–stress and iso–strain assumptions have been accepted for the calculation of composite material elastic properties as providing bounds of the actual material properties. Good agreement with experimental data for elastic modulus has been found for the case of plain weave reinforcement in [11] under iso-stress assumption. The same assumption for stress calculation is used in [21, 22, 24], while the iso-strain assumption is used in [19, 24]. A method different from iso–stress/iso–strain is developed in [16, 19] based on a model of beam on elastic foundation for the load carrying tow, which is expected to represent more accurately the internal mechanics of the fabric reinforcement. However, the beam on elastic foundation model in [16, 19] is developed only for the case of plain weave under uniaxial loading.

As a result of the bending restrained and iso–stress assumptions, the local constitutive relationship at any  $(x, y)$  location of RUC is

$$\left\{ \begin{array}{c} \epsilon_x^0 \\ \epsilon_y^0 \\ \gamma_{xy}^0 \end{array} \right\} (x, y) = [A(x, y)]^{-1} \left\{ \begin{array}{c} N_x \\ N_y \\ N_{xy} \end{array} \right\} \quad (14)$$

where  $\{\epsilon^0\}(x, y)$  is the local strain,  $[A(x, y)]$  is the local in-plane stiffness matrix (8), and  $\{N\}$  is the applied stress. Equation (14) provides the strain field over RUC.

The methodology for stress analysis is based on point–wise CLT. Thus, local stresses in laminate coordi-

nate system in each fill, warp, and matrix constituent of each element in the RUC are

$$\begin{Bmatrix} \sigma_x \\ \sigma_y \\ \sigma_{xy} \end{Bmatrix}_q (x, y) = [\bar{Q}(x, y)]_q \begin{Bmatrix} \epsilon_x \\ \epsilon_y \\ \gamma_{xy} \end{Bmatrix} (x, y) \quad (15)$$

where  $q = f, w, m$  indicates the fill, warp, and matrix, respectively;  $[\bar{Q}(x, y)]_q$  is the reduced transformed stiffness matrix (29) and  $\{\epsilon\}(x, y)$  is the strain vector (14) of the element at the location  $(x, y)$ .

Local stresses in material coordinate system in each element in the RUC are

$$\{\sigma_1, \sigma_2, \sigma_3, \sigma_4, \sigma_5, \sigma_6\}_q^T (x, y) = [T]_q(x, y) \{\sigma_x, \sigma_y, 0, 0, 0, \sigma_{xy}\}_q^T (x, y) \quad (16)$$

where  $q = f, w$  indicates fill and warp, respectively, and  $[T]_q(x, y)$  is the stress rotation matrix (24).

Failure indices at each position  $x, y$ , in the mesh are computed with the maximum stress failure criteria for each fill and warp constituent (position  $z$ ) as

$$\begin{bmatrix} I_1 \\ I_2 \\ I_3 \\ I_4 \\ I_5 \\ I_6 \end{bmatrix}_q = \begin{bmatrix} \sigma_1/F_{1t} \\ \sigma_2/F_{2t} \\ \sigma_3/F_{3t} \\ \sigma_4/F_4 \\ \sigma_5/F_5 \\ \sigma_6/F_6 \end{bmatrix}_q \quad (17)$$

where  $q = f, w$  indicates fill and warp, respectively;  $F_{1t}, F_{2t}, F_{3t}, F_4, F_5, F_6$  are the strength properties of the tow regarded as UD composite with tow fiber volume fraction  $V_t^f$  (see Section 2.1). The strength values  $F_{1t} \cdots F_6$  are either evaluated experimentally or based on micro-mechanical models [2, 37–39].

The failure indices  $I_1 \cdots I_6$  (17) account for six different possible failure modes in the fill/warp constituents:

- $I_1$  – longitudinal tensile failure along 1 axis of the tow (fiber direction),
- $I_2$  – transverse tensile failure along 2 axis of the tow,
- $I_3$  – transverse tensile failure along 3 axis of the tow,
- $I_4$  – shear failure in the (2, 3) plane of the tow,
- $I_5$  – shear failure in the (1, 3) plane of the tow,
- $I_6$  – shear failure in the (1, 2) plane of the tow.

The matrix constituent of each element is also monitored for failure using the von Misses failure criterion.

Local failure in fill, warp, and matrix constituents is checked at each load increment by calculating the failure indices (17). When one mode of failure is detected in any constituent of an element, the stiffness of the respective constituent is reduced according with the detected mode of failure. The stiffness reduction model in [37, Section 8.2] is implemented in the present WF progressive failure model. Thus, the stiffness matrix of a damaged constituent is calculated as

$$C_q = \begin{bmatrix} \tilde{C}_{11}\Omega_1^4 & \tilde{C}_{12}\Omega_1^2\Omega_2^2 & \tilde{C}_{13}\Omega_1^2\Omega_3^2 & 0 & 0 & 0 \\ \tilde{C}_{12}\Omega_1^2\Omega_2^2 & \tilde{C}_{22}\Omega_2^4 & \tilde{C}_{23}\Omega_2^2\Omega_3^2 & 0 & 0 & 0 \\ \tilde{C}_{13}\Omega_1^2\Omega_3^2 & \tilde{C}_{23}\Omega_2^2\Omega_3^2 & \tilde{C}_{33}\Omega_3^4 & 0 & 0 & 0 \\ 0 & 0 & 0 & \tilde{C}_{44}\Omega_2^2\Omega_3^2 & 0 & 0 \\ 0 & 0 & 0 & 0 & \tilde{C}_{55}\Omega_1^2\Omega_3^2 & 0 \\ 0 & 0 & 0 & 0 & 0 & \tilde{C}_{66}\Omega_1^2\Omega_2^2 \end{bmatrix}_q \quad (18)$$

where  $\tilde{C}_{ij}$  are the components of the undamaged (virgin) stiffness matrix; the *integrity tensor*  $\Omega$  is based on the damage tensor  $\mathbf{D}$  as  $\Omega = \sqrt{\mathbf{I} - \mathbf{D}}$ , and  $\mathbf{I}$  is the  $3 \times 3$  unit matrix. The damage tensor  $\mathbf{D}$  is expressed

as function of the damage coefficients  $d_i$  ( $i = 1 \cdots 3$ ) as  $D_{ij} = d_i \delta_{ij}$  (no sum on  $i$ ); and  $\delta_{ij}$  is the Kronecker delta function.

Initially, the damage coefficients  $d_i$  ( $i = 1 \cdots 3$ ) are set to zero (non-damaged material). When damage is detected, the damage coefficients  $d_i$  are selectively assigned non-zero values according to the detected mode of failure:

- $d_1$  for failure affecting the 1 principal direction of the tow (i.e., failure mode 1),
- $d_2$  for failure affecting the 2 principal direction of the tow (i.e., failure mode 2, 4 or 6),
- $d_3$  for failure affecting the 3 principal direction of the tow (i.e., failure mode 3 or 5).

The assigned values of the damage coefficients  $d_i$  when failure is detected in one of the the six failure modes are:  $d_1 = 0.99$ ,  $d_2 = d_3 = 0.8$ . The reason for assigning a lower value to  $d_2$  and  $d_3$  is because the implemented stiffness reduction model considers one single damage coefficient ( $d_2$  or  $d_3$ ) for multiple modes of failure (2, 4, 6 and 3, 5, respectively). However, due to friction on the local damage surfaces, it is expected that the material keeps some of its shear stiffness when failure takes place in a transverse mode (either tensile or shear), and the lower values  $d_2 = d_3 = 0.8$  account for this observation. Another approach of the same method of stiffness reduction coefficients would be to assign different  $d_i$  ( $i = 1 \cdots 6$ ) coefficient for all 6 modes of failure  $I_1 \cdots I_6$  as in [30, 31]. When one damage mode is detected in one constituent of an element, and the stiffness of that constituent is degraded accordingly, stress redistribution to the other constituents of the element is accounted for by iterating at the same load level.

Under tensile loading, early mode 1 failure is encountered in elements of RUC due to the geometrical features of RUC (undulation) combined with the ‘iso-stress’ load distribution. In this case, the stiffness reduction coefficient of the tow is accordingly set to  $d_1$ . Then, the longitudinal load is increased on undamaged elements situated along lines of the discretizing mesh parallel to the longitudinal load direction. The internal increase in longitudinal load on the undamaged elements is made proportional with the dimension of the damaged element. For example,  $N'_x = N_x \cdot L_y / \delta y$  for the case of longitudinal loading along  $x$  direction of the RUC (see Fig. 3), where  $N_x$  is the external longitudinal applied load,  $N'_x$  is the internal longitudinal load on the undamaged elements considering the load redistribution effect,  $L_y = n_g w_f$  is the transverse dimension of the RUC, and  $\delta y$  is the transverse dimension of the element featuring longitudinal failure in its longitudinal constituent. This load redistribution mechanism is considered only for the case of longitudinal loading, not for shear loading. The overall effect of load redistribution is accounted for by iterating at the same load level.

The overall material behavior after failure initiation is evaluated by calculating the global in-plane stiffness matrix  $[A]$  in (10) considering the reduced stiffness matrix (18). The RUC overall deformations are

$$\{\epsilon_x^0, \epsilon_y^0, \gamma_{xy}^0\}^T = [A]^{-1} \{N_x, N_y, N_{xy}\}^T \quad (19)$$

and overall stresses are

$$\{\sigma_x, \sigma_y, \sigma_{xy}\}^T = \{N_x/h_c, N_y/h_c, N_{xy}/h_c\}^T \quad (20)$$

where  $\{N\}$  is the applied load and  $h_c = h_f + h_w + h_r$  is the ply thickness (see Fig. 1.)

The final failure for longitudinal loading is predicted when one element of each line of elements along the load direction have failed in mode 1. The final failure for in-plane shear loading is predicted when all the elements in the mesh have failed in shear mode.

### 3 Results

A parametric study predicting thermo-elastic constants and strength is presented in the following. The material system considered is E-Glass/Epoxy with constituents properties given in Table 1 [16]. The study has the objective to analyze the influence of two principal classes of parameters on the the material properties:

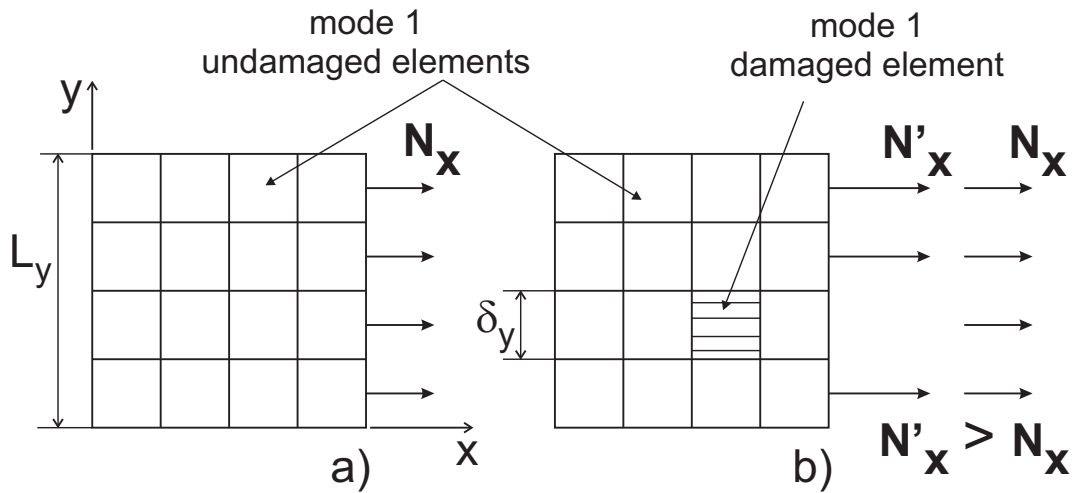


Figure 3: Load redistribution due to mode 1 damage.

Table 1: Mechanical properties of E-Glass fibers and Epoxy matrix ( [16])

Property	Symbol	Units	Value
<b>E-Glass fiber</b>			
Modulus	$E^f$	GPa	72.0
Poisson's ratio	$\nu^f$		0.3
Strength (manufacturer specification)	$F^f$	MPa	3450.0
Strength ( <i>in-situ</i> )	$F_{is}^f$	MPa	1995.0
Thermal Expansion Coefficient	$\alpha^f$	$\mu\epsilon/^\circ C$	5.4
Moisture Expansion Coefficient	$\beta^f$	$\epsilon$	0.0
Density	$\rho^f$	$g/cm^3$	2.62
<b>Epoxy matrix</b>			
Modulus	$E^m$	GPa	3.5
Poisson's ratio	$\nu^m$		0.35
Tensile Strength (bulk, manufacturer specification)	$F_t^m$	MPa	60.0
Tensile Strength ( <i>in-situ</i> )	$F_{is}^m$	MPa	36.6
Shear Strength (bulk, manufacturer specification)	$S^m$	MPa	100.0
Shear Strength ( <i>in-situ</i> )	$F_{is}^m$	MPa	43.0
Thermal Expansion Coefficient	$\alpha^m$	$\mu\epsilon/^\circ C$	63
Moisture Expansion Coefficient	$\beta^m$	$\epsilon$	0.33
Density	$\rho^m$	$g/cm^3$	1.17

- Parameters defining the tow geometry:  $a_f, g_f, h_f, a_w, g_w, h_w$ , and
- Parameters defining the weaving pattern of the fabric reinforcement:  $n_g, n_s, n_i$ .

A large variety of twill/satin weaving styles can be described by the  $n_g/n_s/n_i$  combination of the weaving pattern parameters, as shown in *Part I* [33]. Comparison with available experimental data is presented last, in section 3.4.

In this section, for simplicity, the fill and warp geometrical parameters are taken to be equal to each other. Therefore, the subscripts  $f, w$ , are not needed, and the parameters are thus referred simply as tow width  $a$ , tow thickness  $h$ , and gap  $g$ .

A range of gap to tow width  $g/a = (0.05 - 1)$  and tow thickness to tow width  $h/a = (0.05 - 0.5)$  is considered for the parametric analysis, for fixed tow width  $a = 2\text{ mm}$ . The influence of  $g/a$  and  $h/a$  is studied for the 2/1/1 weaving pattern (i.e., plain weave).<sup>2</sup> The influence of weaving pattern is studied for the case of twill family  $n_g/1/1$  with  $n_g = (1 \cdots 11)$ .

For each of the aforementioned cases, two situations are presented: 1) constant *tow* fiber volume fraction  $V_t^f = 0.7$  and 2) constant *overall* fiber volume fraction  $V_o^f = 0.35$ . Constant tow fiber volume fraction is achievable by controlling the compaction level during composite material manufacturing. Constant overall fiber volume fraction is more difficult to achieve in practice due to the complex 3D configuration of the composite material architecture, but it is presented here in order to build a complete picture of the material behavior. Note that an explicit relationship exists (6) between  $V_t^f$  and  $V_o^f$ .

The subscript notations  $m$  and  $M$  are used in the following for the *minimum* and *maximum* values of the  $g$  and  $h$  variables, respectively, at the extremes of their variation intervals.

Constituent *in-situ* strength properties listed in Table 1 are different from manufacturer specifications—longitudinal strength values are different due to fiber misalignment [2, Sect. 4.4.3]; transverse strength values are different due to imperfections [2, Sect. 4.4.4]. Because of this, the *in-situ* strength values of the constituents have to be back-calculated based on known (experimental) strength values of UD composites at a given fiber volume fraction and micro-mechanical strength models, including in this way the influence of manufacturing parameters. The back-calculated strength values are regarded as *in-situ* strengths. These values are then the input to the analytical model.

### 3.1 Fiber volume fraction

The influence of the tow geometrical parameters  $g/a$  and  $h/a$  on overall fiber volume fraction  $V_o^f$  at constant tow fiber volume fraction  $V_t^f = 0.7$  is presented in Fig. 4. The lines with square and circle symbols depict overall fiber volume fraction as a function of gap  $g/a$  for constant thickness  $h$ , so their abscissa must be read on the bottom horizontal axis. The lines with triangular symbols depict overall fiber volume fraction as a function of thickness  $h/a$  for constant gap  $g$ , so their abscissa must be read on the top horizontal axis.

The curves for minimum thickness  $h_m$  and maximum thickness  $h_M$  display a pronounced downward trend because the gap is made out entirely of pure matrix, thus the larger the gap the lower the overall fiber volume fraction. These two curves are not very different from each other because the thickness plays a minor role in the overall volume fraction. Such minor role is linked to the increased undulation as the thickness grows, so the curve with square symbols (maximum thickness  $h_M$ ) decreases a bit faster than the curve with circle symbols (minimum thickness  $h_m$ ).

A large difference in overall fiber volume fraction can be seen between the curves with minimum gap  $g_m$  and maximum gap  $g_M$  for the whole range of  $h/a$ . Therefore, we can conclude that the overall fiber volume fraction is very sensitive to the magnitude of the gap and almost insensitive to the thickness, and thus almost insensitive to the undulation.

The influence of harness  $n_g$  on overall fiber volume fraction  $V_o^f$  at constant tow fiber volume fraction  $V_t^f = 0.7$  is presented in Fig. 5. It can be seen that harness has some influence only at low gap  $g_m$  and high thickness  $h_M$ . At constant tow fiber volume, the overall fiber volume decreases with harness. This can be explained as follows. The tow length is longer in the region with undulation than in the region without

<sup>2</sup>Note that the plain weave 2/1/1 is generated by the general code used for all other examples, which also is capable of generating any  $n_g/1/n_i$  and  $n_g/n_s/1$  weave.

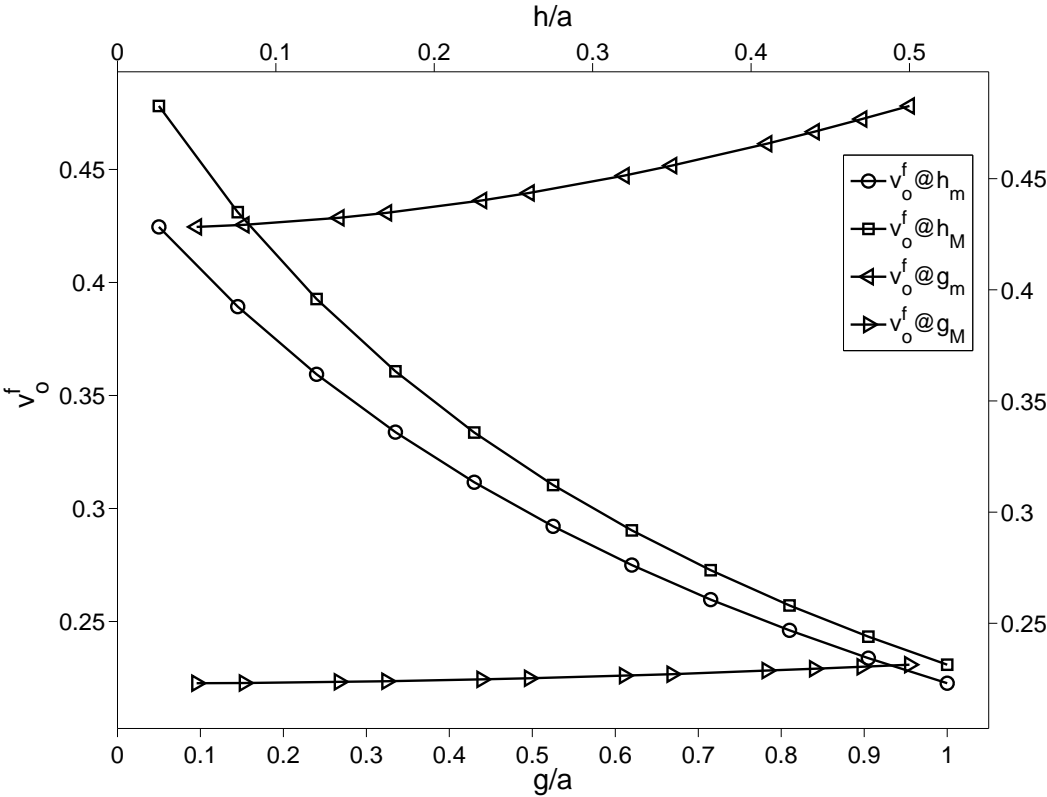


Figure 4: Variation of overall fiber volume fraction with tow geometrical parameters (constant  $V_t^f = 0.7$ ).

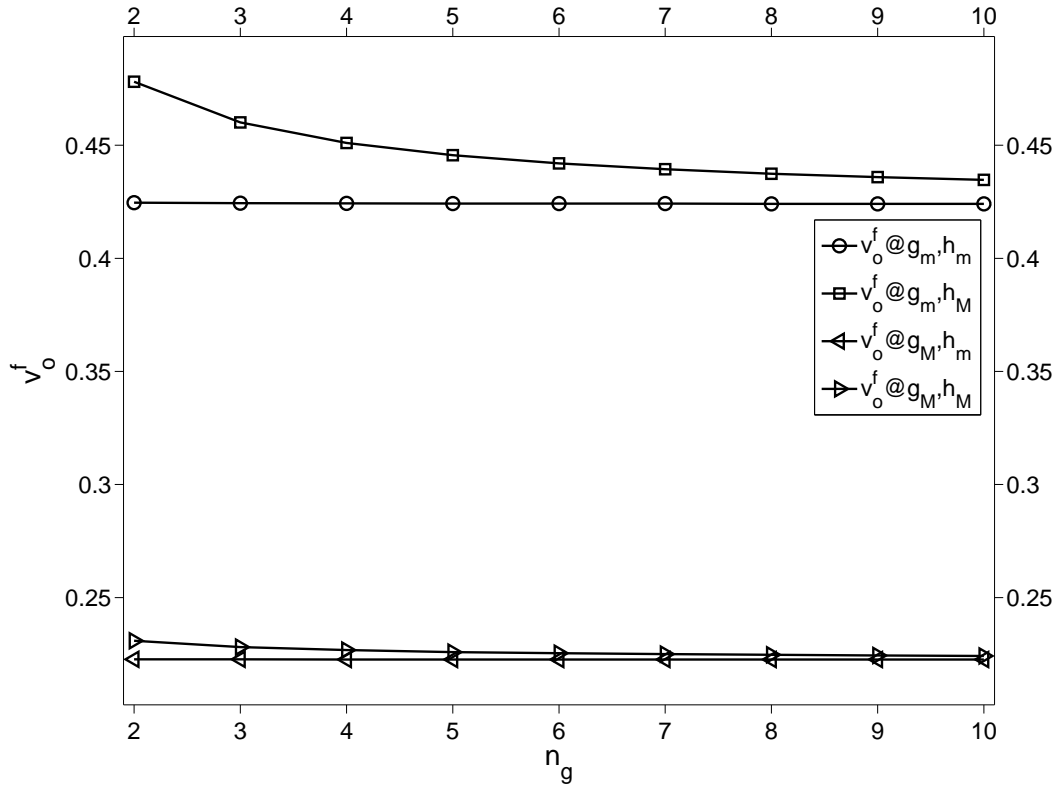


Figure 5: Variation of overall fiber volume fraction with weaving style (constant  $V_t^f = 0.7$ ).

undulation (see Fig. 2). The tow volume is simply the tow length times the tow area. The undulation is concentrated over the interlacing region, which for a  $n_g/1/1$  is only one tow ( $n_i = 1$ ) out of  $n_g$  tows along each direction, fill and warp, in the RUC. Therefore, the higher the harness, the less percentage of RUC volume is comprised by undulating tows, and by virtue of (5) the volume fraction of tows in the RUC, namely  $V_{meso}$ , decreases with harness. Then, by virtue of (6) rewritten as  $V_o^f = V_t^f V_{meso}$ , the overall fiber volume fraction decreases also with harness.

It is interesting to note that the large difference in  $V_o^f$  between the curves in Fig. 5 (circle and square symbols vs. triangular symbols) is almost entirely attributable to the gap, not to the thickness. For any harness, overall fiber volume fraction is controlled by the gap, thus reinforcing the conclusions drawn from Fig. 4. The higher the gap, the lower the volume fraction. In hindsight, this result seems to be obvious, which begs a reminder that the conclusion herein was reached from the model results, which not only are able to predict the correct trend but also to quantify the influence of harness, gap, thickness, and pitch for a broad variety of twill, satins, and of course plain weave fabrics.

The influence of harness  $n_g$  on *tow* fiber volume fraction  $V_t^f$ , at constant overall fiber volume fraction  $V_o^f = 0.35$  is presented in Fig. 6. The trend is the opposite of that observed in Fig. 5. At constant overall fiber volume, the tow fiber volume increases with harness. This is the opposite effect to that observed in Fig. 5 and it can be explained in the same way. At constant overall fiber volume, the less length of tow there is, the higher it's fiber volume fraction must be in order to keep the overall fiber volume constant. As explained before, the higher the harness, the higher the percentage of volume is made of flat tows, the later having shorter tow length.

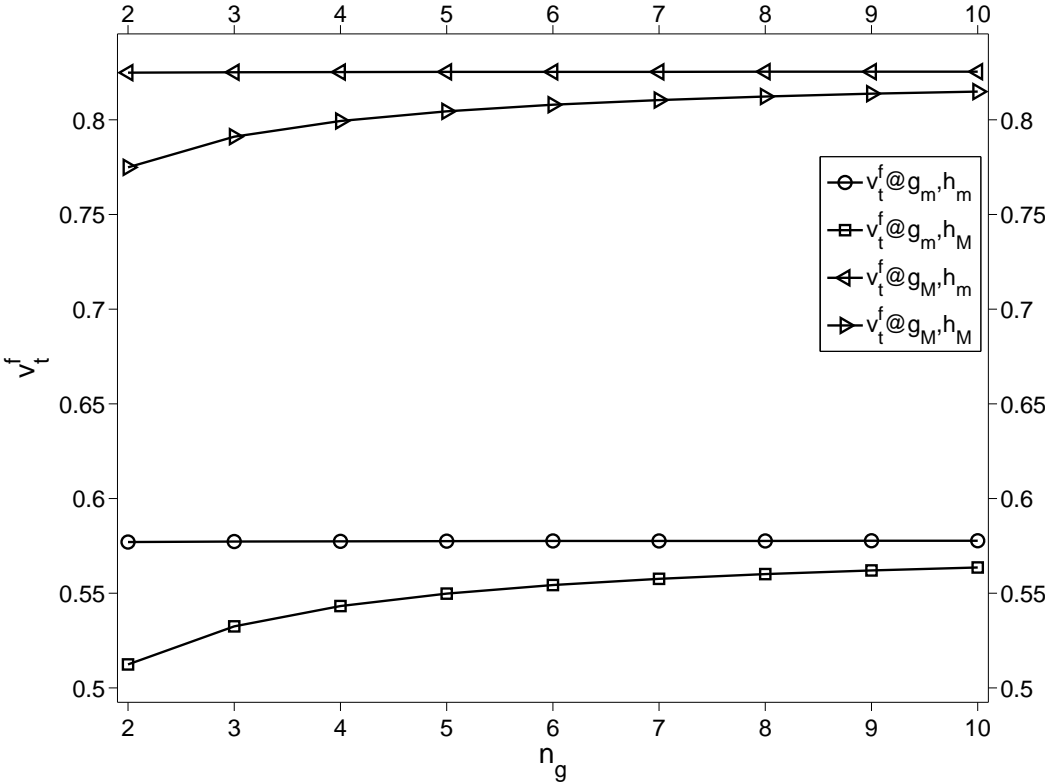


Figure 6: Variation of tow fiber volume fraction with weaving style (constant  $V_o^f = 0.35$ ).

### 3.2 Thermo-elastic material properties

The influence of the (dimensionless) gap  $g/a$  on thermo-elastic properties of the composite material, at constant tow fiber volume fraction  $V_t^f = 0.7$ , is presented in Fig. 7 and Fig. 8. The undesired knock-down of material elastic moduli due to dimensionless gap  $g/a$  is notable in Fig. 7. The variation of Poisson ratio and CTE can be observed in Fig. 8.

Regarding Young's modulus  $E_x$  in Fig. 7, it can be observed that the gap  $g/a$  has higher influence at small thickness, as it is displayed by the curve at minimum thickness  $h_m$ . This is due to the undulation that is less at small thickness  $h_m$  for the same tow width  $a$ . The larger the gap, the lower the Young's modulus. The in-plane shear modulus  $G_{xy}$  is equally sensitive to gap whether the thickness, and thus the undulation, are small  $h_m$  or large  $h_M$ . The larger the gap, the lower the shear modulus.

The values of Poisson ratio  $\nu_{xy}$  and CTE  $\alpha_x$  shown in Fig. 8 are quite sensitive to gap. The larger the gap, the larger the CTE and Poisson's; both being deleterious effects of the gap.

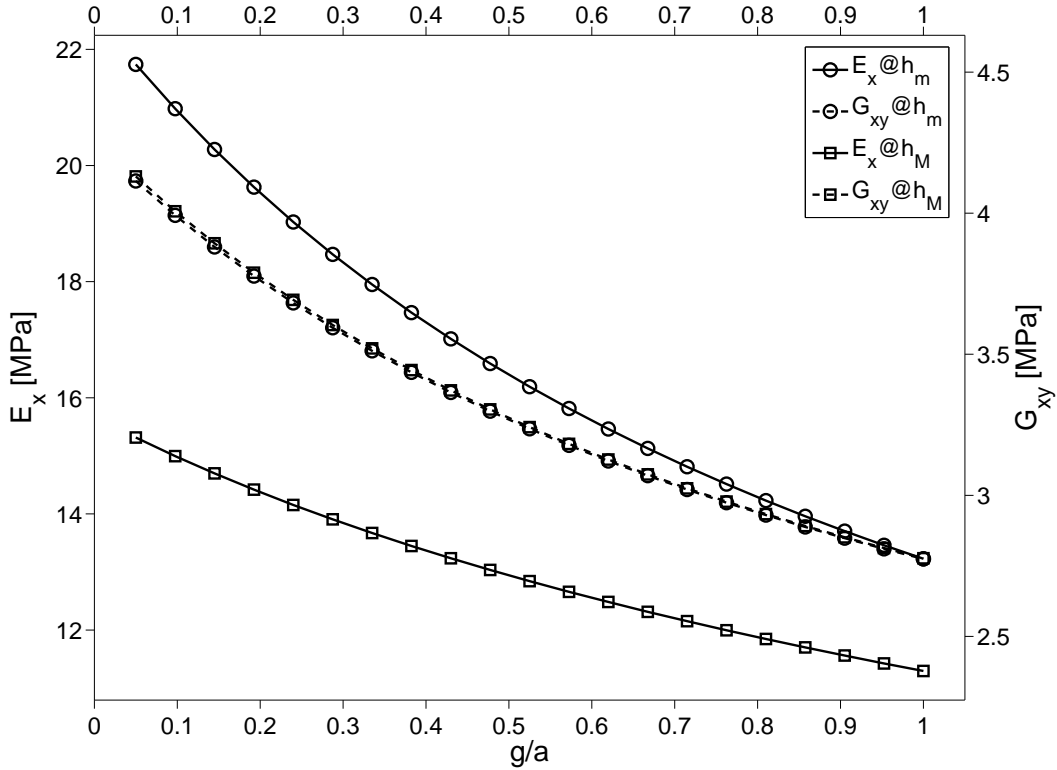


Figure 7: Variation of Young and shear modulus with tow geometrical parameters (constant  $V_t^f = 0.7$ ).

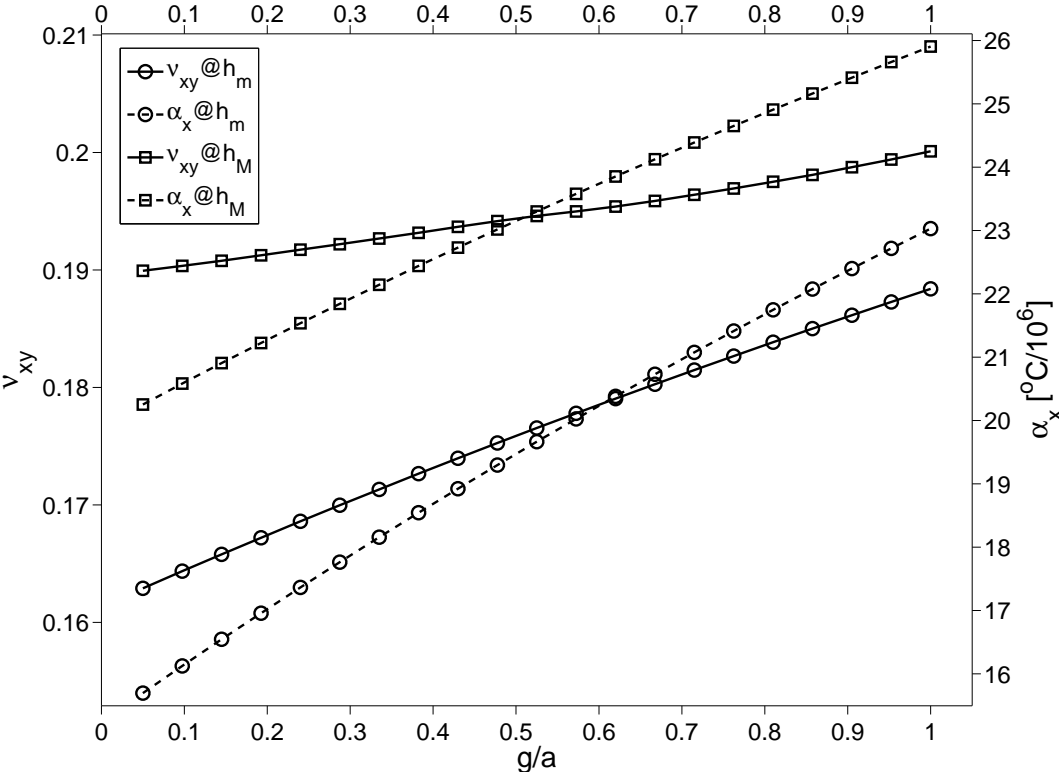


Figure 8: Variation of Poisson ratio and CTE with tow geometrical parameters (constant  $V_t^f = 0.7$ ).

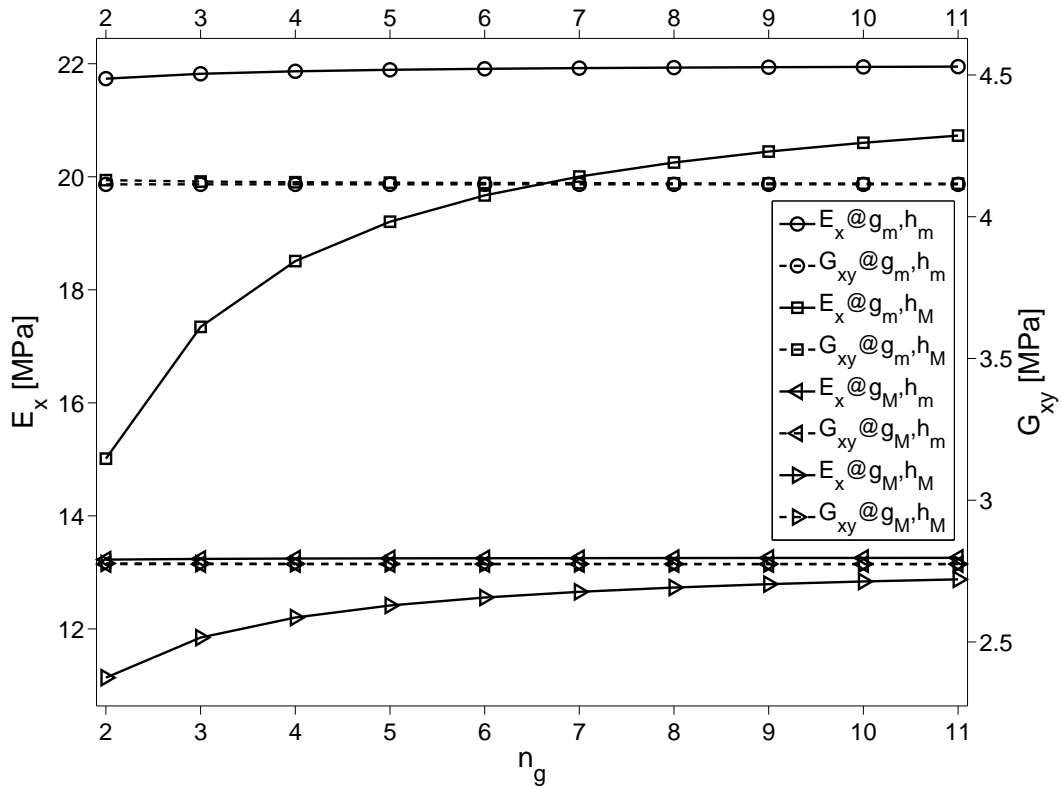


Figure 9: Variation of Young and shear modulus with weaving style (constant  $V_t^f = 0.7$ ).

The influence of hardness  $n_g$  on Young's modulus  $E_x$  and shear modulus  $G_{xy}$ , at constant tow fiber volume fraction  $V_t^f = 0.7$ , is illustrated in Fig. 9. The shear modulus  $G_{xy}$  is shown to be virtually insensitive to harness. The Young modulus varies the most at minimum gap  $g_m$  and maximum thickness  $h_M$ . Also, the Young modulus varies significantly at maximum gap  $g_M$  and maximum thickness  $h_M$ . To understand this, please refer to Fig. 10, which depicts the case  $n_g/n_s/n_i = 7/1/1$ . One can see that the reinforcement consists of two distinct regions: the interlacing regions and long regions where the tows are flat and straight. On a  $n_g/1/1$  weave, the higher the harness  $n_g$ , the longer the flat regions. These flat regions contribute more to the Young's modulus than the interlacing regions, because the latter have undulation. Note on Fig. 9 that the plain weave ( $n_g = 2$ ) loses almost 30% of the modulus when compared to a high hardness case.

Also in Fig. 9, note that Young's modulus is higher when the gap is small (square symbols for a gap  $g_m$ ) than when the gap is large (triangular symbols for a gap  $g_M$ ). This is due to the gap lowering the overall volume fraction, which has a direct effect on lowering Young's modulus. Noticeable variation in CTE and Poisson's ratio are observed on Fig. 11 as well. Lower CTE and lower Poisson's ratio are achieved for high hardness because, being both fiber dominated, they follow exactly the opposite trend as Young's modulus. With the fiber modulus larger than the matrix modulus, and fiber CTE and Poisson's ratio smaller than those of the matrix, the trends for modulus must be opposite to that of CTE and Poisson's ratio. Again, not only logical trends, but also quantitative values, are predicted by the proposed formulation.

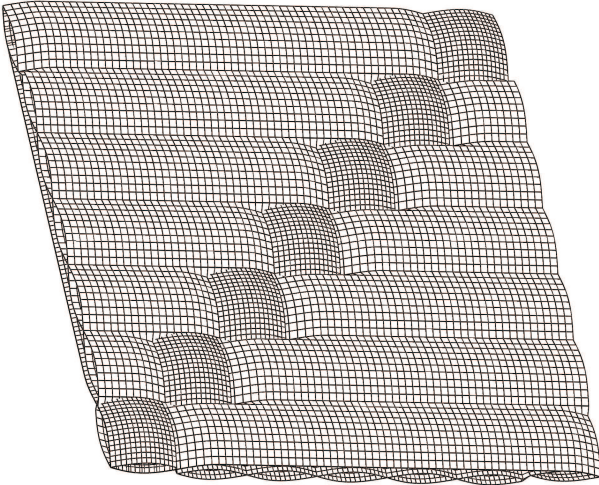


Figure 10: Reinforcement weave described by  $n_g/n_s/n_i = 7/1/1$ .

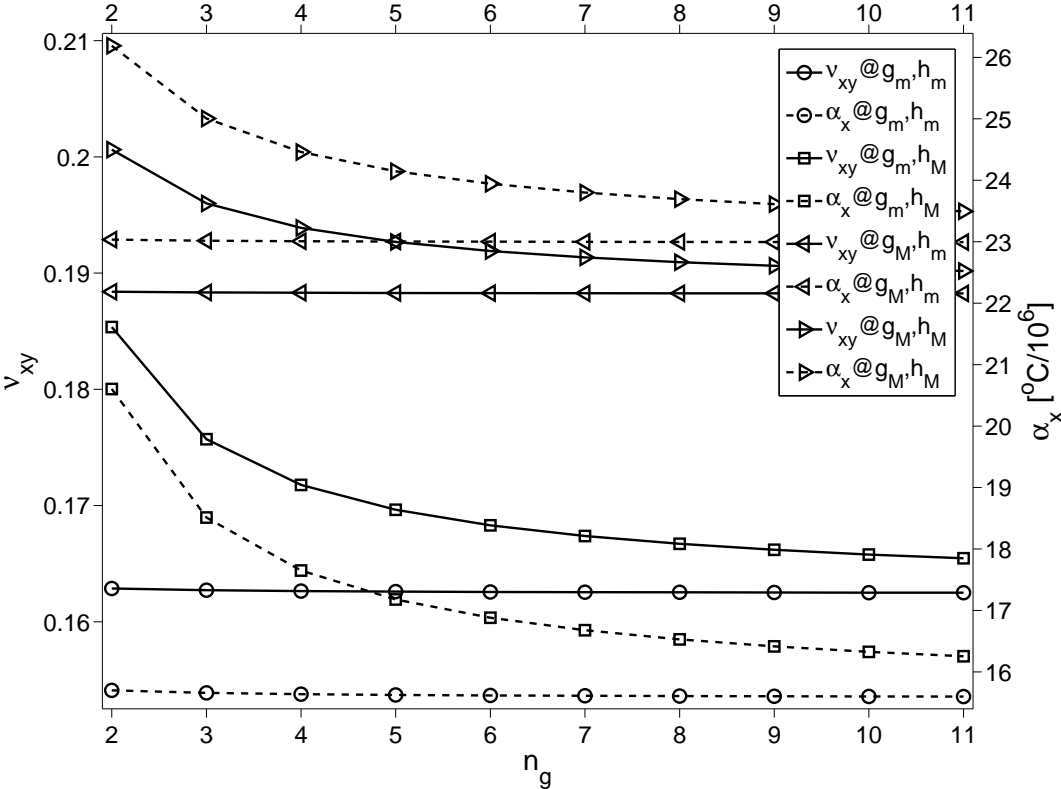


Figure 11: Variation of Poisson ratio and CTE with weaving style (constant  $V_t^f = 0.7$ ).

The trends observed in Fig. 9 and Fig. 11 for constant *tow fiber volume fraction*  $V_t^f = 0.7$ , basically reproduce themselves onto Fig. 12 and Fig. 13 for constant *overall fiber volume fraction*  $V_o^f = 0.35$ , with some differences. Still, a noticeable knock-down in Young's modulus is observed in Fig. 12 for low harness (e.g., plain weave). The undesirable increase in CTE and Poisson's ratio is also observed in Fig. 13 for low harness. The explanation for this behavior is identical to that offered for the previous case.

Note that in Fig. 9, the Young's modulus curve for low gap ( $g_m$ , square symbols) is above the Young's modulus curve for large gap ( $g_M$ , triangular symbols). This is because, at constant *tow fiber volume*, a large gap decreases the overall fiber volume, thus the modulus. On the contrary, in Fig. 12, the Young's modulus curve for low gap ( $g_m$ , square symbols) is below the Young's modulus curve for large gap ( $g_M$ , triangular symbols). This is because, at constant *overall fiber volume*, a large gap forces the tow fiber volume to increase, increasing the longitudinal modulus of the tow, thus the modulus of the composite.

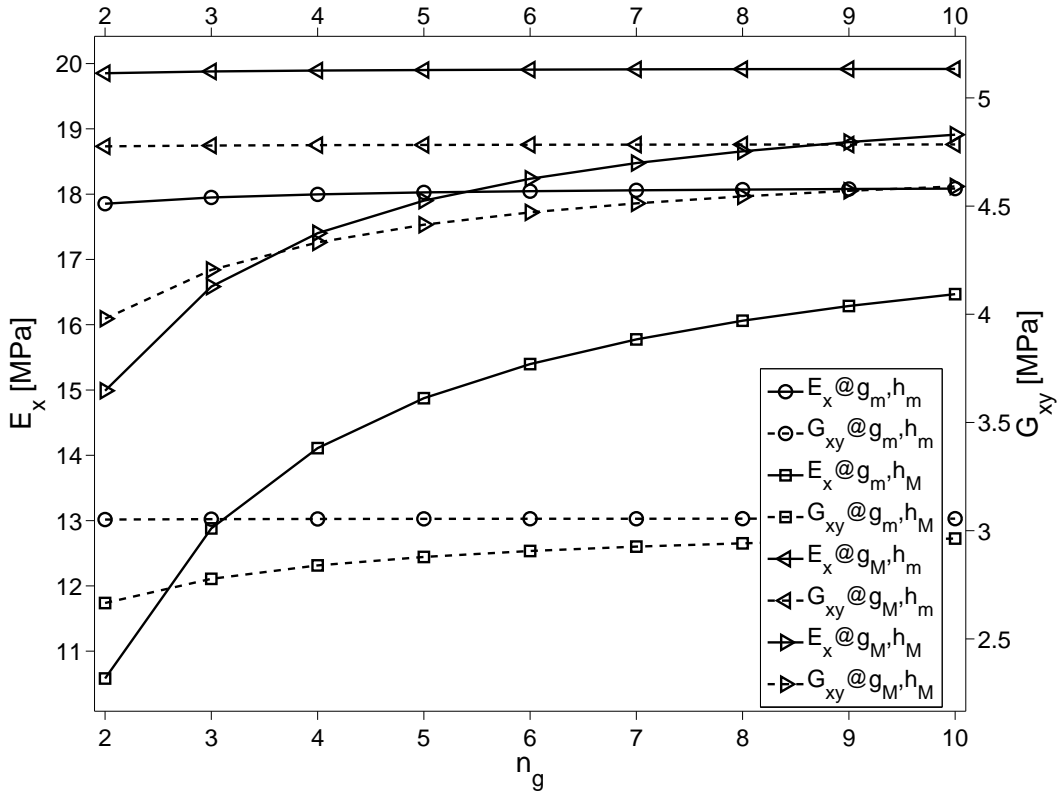


Figure 12: Variation of Young and shear modulus with weaving style (constant  $V_o^f = 0.35$ ).

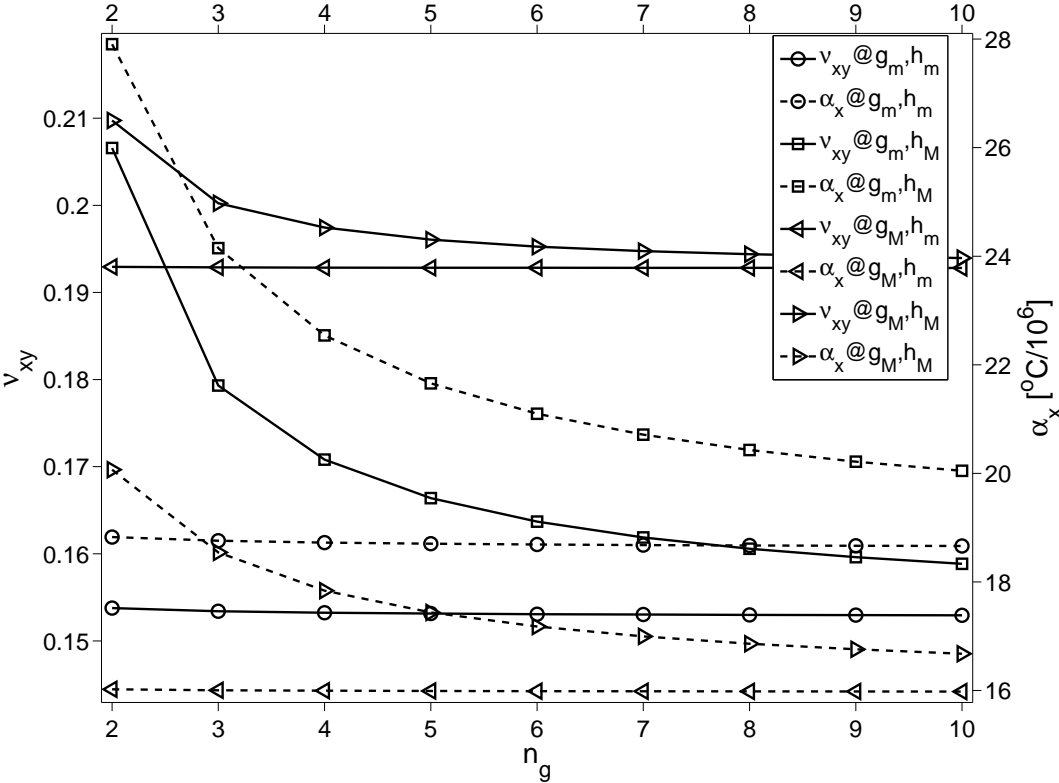


Figure 13: Variation of Poisson ratio and CTE with weaving style (constant  $V_o^f = 0.35$ ).

Table 2: Longitudinal tensile and shear strength of the laminate. WF: present formulation, CP: cross-ply approximation, UD: unidirectional approximation.

ng	Fig. 14 uniaxial $F_{xt}$ [MPa]			Fig. 15 uniaxial $F_{xt}$ [MPa]			Fig. 16 uniaxial $F_{xt}$ [MPa]				Fig. 17 shear $F_{xy}$ [MPa]	
	WF	CP	UD	WF	CP	UD	Exp.	WF	CP	UD	Exp.	WF
2	320	451.4	499.7	255	380.6	412.1	318	325	428.09	490.74	35.2	32.72
5	320	451.1	499.7	265	380.6	422.3	-	-	-	-	-	-
8	320	451.0	499.7	265	380.6	424.9	-	-	-	-	-	-

### 3.3 Progressive failure and strength

Stress–strain curves for weaving styles (plain weave  $n_g = 2$ , and twill  $n_g = 5, 8$ ), at constant *tow* fiber volume fraction  $V_t^f = 0.7$ , are presented in Fig. 14. At such high *tow* fiber volume fraction, the influence of the the weaving style is small. The fabric configuration is  $a = 2\text{ mm}$ ,  $g = 0.1\text{ mm}$ ,  $h = 0.1\text{ mm}$ . The loading case is uniaxial tension along the fill direction. For this case, predicted strength values are insensitive to harness  $n_g$  and weaving style (Table 2).

Stress–strain curves for weaving styles (plain weave  $n_g = 2$ , and twill  $n_g = 5, 8$ ), at constant *overall* fiber volume fraction  $V_o^f = 0.35$ , are presented in Fig. 15. The fabric configuration is  $a = 2\text{ mm}$ ,  $g = 0.1\text{ mm}$ ,  $h = 0.64\text{ mm}$ . The loading case is uniaxial tension along the fill direction. The stress–strain plot for twill ( $n_g = 5, 8$ ) is different than for plain weave ( $n_g = 2$ ). The ultimate strength predicted by the proposed method (WF) are different also, but not much, as it can be seen in Table 2. On the same table, notice how unconservative the approximate methods are, namely the cross-ply and unidirectional approximations (see section 2.1). The CP and UD strength values in Table 2 have been calculated based on the ply discount method implemented in [40], and micro-mechanical strength models for UD composites [2, 38], respectively.

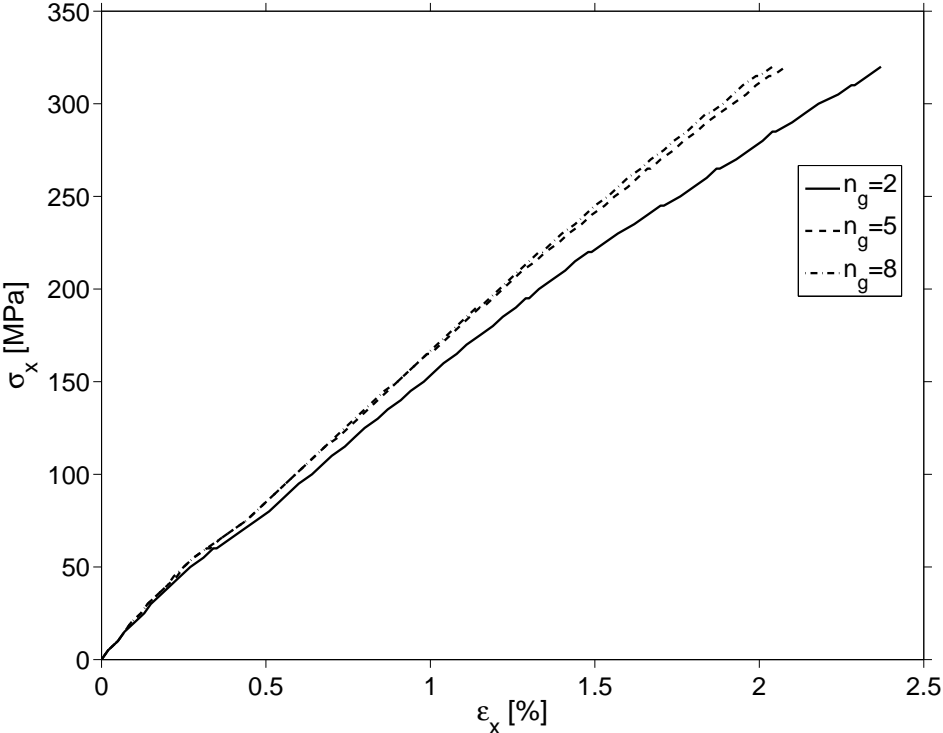


Figure 14: Constitutive behavior up to failure for different  $n_g/1/1$  weaving patterns, uniaxial tensile loading case (constant  $V_t^f = 0.7$ ).

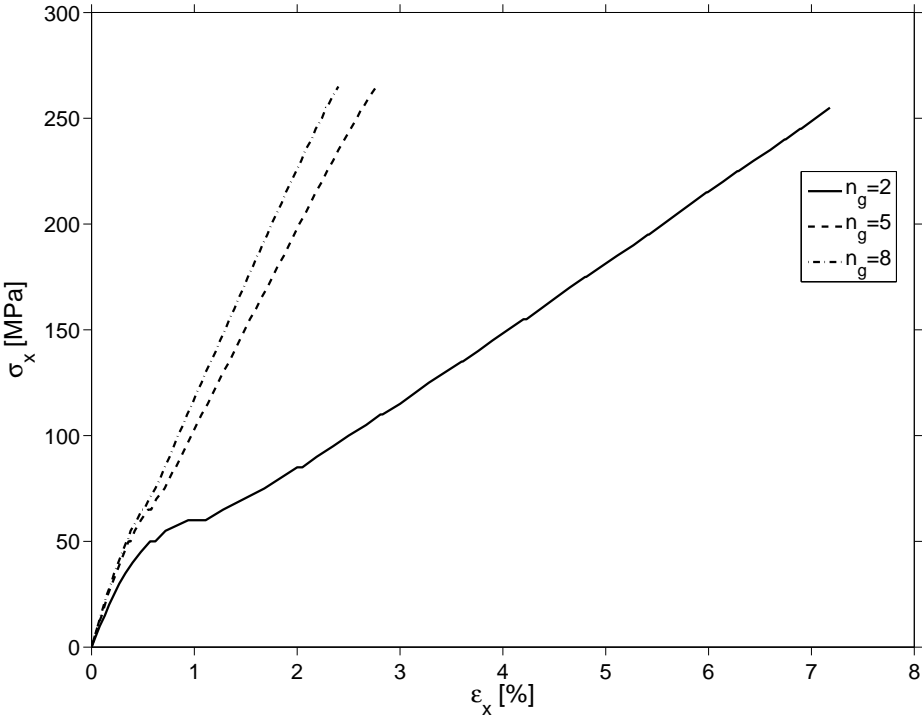


Figure 15: Constitutive behavior up to failure for different  $n_g/1/1$  weaving patterns, uniaxial tensile loading case (constant  $V_o^f = 0.35$ ).

### 3.4 Comparison with Experimental Data

The predicted constitutive behavior up to failure is compared to experimental data in Fig. 16 and Fig. 17. Comparison for the case of uniaxial tensile loading experiments [16] is shown in Fig. 16 and Table 2 for the following fabric configuration

$$\begin{aligned} a_f &= 0.68 \text{ mm}, g_f = 0.04 \text{ mm}, h_f = 0.09 \text{ mm}, \\ a_w &= 0.62 \text{ mm}, g_w = 0.10 \text{ mm}, h_w = 0.09 \text{ mm}, V_o^f = 0.40, \end{aligned}$$

Comparison for the case of in-plane shear loading experiments [5] is shown in Fig. 17 and Table 2 for the following fabric configuration

$$a_f = a_w = 0.45 \text{ mm}, g_f = g_w = 0.30 \text{ mm}, h_f = h_w = 0.048 \text{ mm}, V_o^f = 0.23.$$

Good agreement between experimental data and results predicted with the present formulation (WF) can be observed for both tensile and shear loading. Note that no experimental values are available for  $n_g > 2$ . Also note that the approximate methods CP and UD are not able to compute an estimate for the shear strength reported in and Table 2 (Fig. 17.)

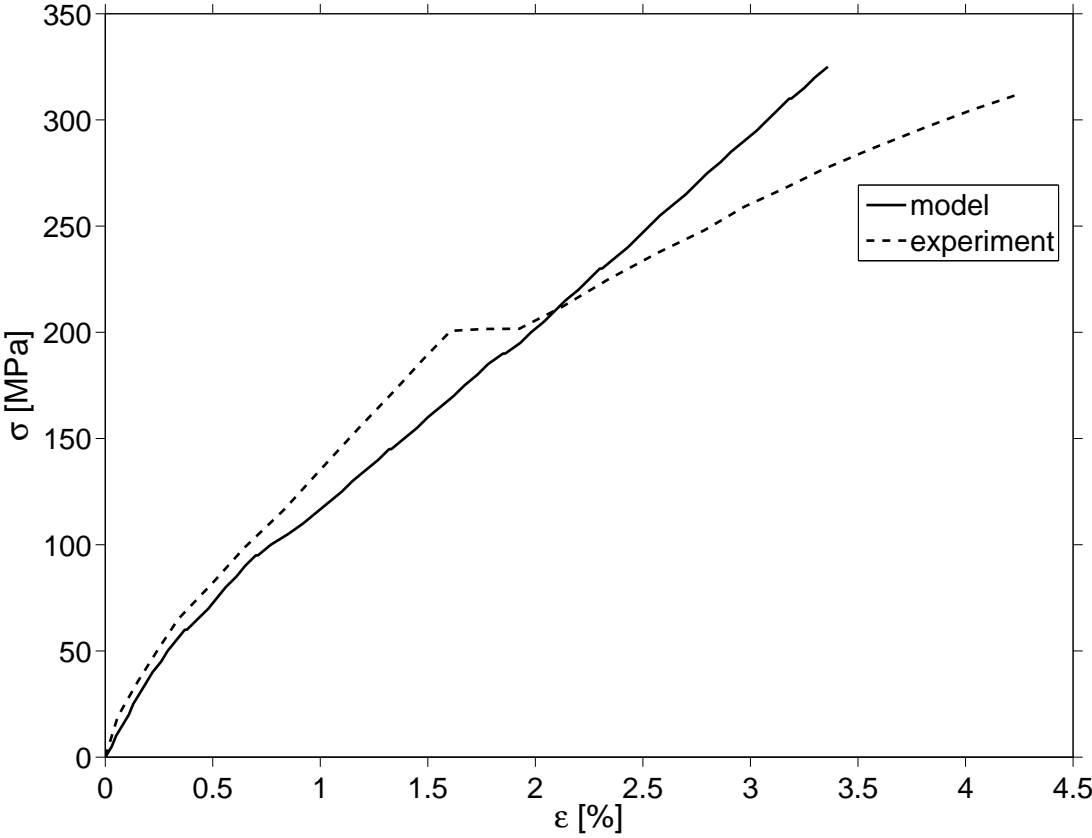


Figure 16: Predicted vs. experimental [5] uniaxial tensile loading of 2/1/1 plain weave reinforced composite.

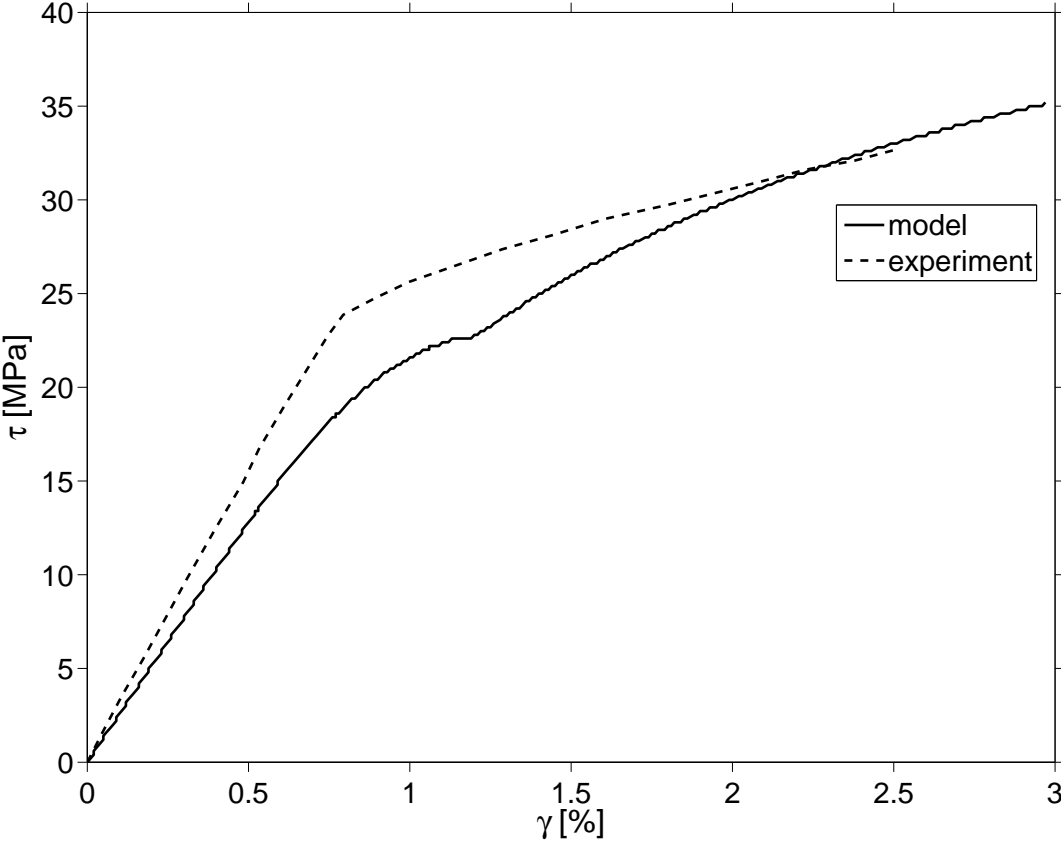


Figure 17: Predicted vs. experimental [16] in-plane shear loading of 2/1/1 plain weave reinforced composite.

## 4 Conclusions

When the tow fiber volume fraction is constant, the overall fiber volume fraction decreases rapidly with increasing gap (Fig. 4) and to some extent with harness (Fig. 5). The elastic constants are highly influenced by the fiber volume fraction, thus gap (Fig. 7). Elastic constant are also affected by undulation, which is shown to be increased by both higher gap and higher tow thickness (Fig. 9). As expected, increasing  $g/a$  and  $h/a$  values knock down the thermoelastic properties of the composite. A larger gap  $g/a$  increases undulation and the volume of pure matrix pockets. Tow thickness  $h/a$  increases undulation as well. The shear modulus is not influenced by undulation (represented by  $h/a$ ) but it is only influenced by the gap  $g/a$ , which reveals a direct dependency to the fiber volume fraction, not to the geometry of the tow (Fig. 9). On the other hand, Young's modulus, Poisson's ratio, and CTE behave similarly; they are all influenced by undulation and fiber volume alike.

From the thermo-elastic material properties point of view, the ideal reinforcing weave is one with minimum gap and minimum undulation. However, other material properties such as drapeability or manufacturing constraints may require a larger gap or larger tow thickness, both of which will have an undesirable effect on the material properties. For this cases, it is important to note the trend in Fig. 9 – 13, which reveals that considerable improvement in material properties at high tow thickness values can be achieved by *modifying the weaving style toward higher harness  $n_g$* .

The shift  $n_s$  and interlacing  $n_i$  are defined in *Part I*. Their influence on composite properties was found to be negligible. Identical results are obtained for  $n_g/1/1$ ,  $n_g/n_s/1$ , and  $n_g/1/n_i$  weaving classes, for all values of  $n_s, n_i$ . Only the harness  $n_g$  has an effect on properties, as shown in this paper. However, the shift and interlacing do have an effect on the drapeability, which may therefore be exploited advantageously since, as it has been noted, *they do not affect the properties of the composite*. Additionally, shift and interlacing have an influence on the location of the maximum undulation  $\theta_{max}$ , thus the stress concentration, and consequently on the location of failure initiation.

Harness, tow thickness, and gap influence the failure initiation load, the location of initiation inside the RUC, the mode of initial failure, and the sequence of progressive failure. The initiation and progressive failure affects the shape of the nonlinear stress-strain plot due to degradation of the elastic constants, as it is shown in Figs. 14– 15. Furthermore, it has been found that *the governing parameter for the ultimate strength value under uniaxial tensile loading is the tow fiber volume fraction  $V_t^f$* . This can be inferred from Table 2, where the same strength value is predicted for three weaving styles having the same tow fiber volume fraction (column 1). Slight differences among the strength values on the second column in the table are due to slightly different values of tow fiber volume fraction obtained by imposing constant overall fiber volume fraction for the three weaving configurations reported in column 2 of the same table. Similar nonlinear behavior and trends, obtained by finite element analysis, for different weaving styles under constant overall fiber volume fraction are reported in [31]. The approximate methods CP and UD were found to be unreliable.

In summary, the formulation proposed is capable of quantifying the effects of fiber volume fraction, weave style (namely harness, shift, and interlacing), as well as tow width, tow thickness, and gap (which combined with harness define the pitch of the fabric) for broad families of weaving patterns such as twill and satin, including plain weave as a particular case. The predicted trends are in agreement with the physics of the problem and are further corroborated by similar conclusions from other works in the literature and by comparison to experimental data for those few cases, notably for plain weave, for which such data exists.

## Appendix 1: Mechanical properties of tows inside of the composite material

The following equations regarding hygro-thermo-elastic properties of individual tows are based on [2, 11, 37]. The 3D compliance matrix of tow regarded as UD composite in material c.s. is

$$S = \begin{pmatrix} 1/E_{11} & -\nu_{21}/E_{22} & -\nu_{31}/E_{33} & 0 & 0 & 0 \\ -\nu_{12}/E_{11} & 1/E_{22} & -\nu_{32}/E_{33} & 0 & 0 & 0 \\ -\nu_{13}/E_{11} & -\nu_{23}/E_{22} & 1/E_{33} & 0 & 0 & 0 \\ 0 & 0 & 0 & 1/G_{23} & 0 & 0 \\ 0 & 0 & 0 & 0 & 1/G_{13} & 0 \\ 0 & 0 & 0 & 0 & 0 & 1/G_{12} \end{pmatrix} \quad (21)$$

where  $E_{ij}, \nu_{ij}, G_{ij}$  are the engineering elastic constants of the UD tow calculated through micro-mechanical models [2, 38, 41] at tow fiber volume fraction  $V_t^f$  (see Section 2.1).

The rotation matrices from material (1, 2, 3) to RUC ( $x, y, z$ ) c.s. are defined by the following relations for fill and warp tows, respectively

$$\Theta_f(x, y) = \begin{pmatrix} l_1 & m_1 & n_1 \\ l_2 & m_2 & n_2 \\ l_3 & m_3 & n_3 \end{pmatrix} = \begin{pmatrix} \cos \theta_f & 0 & \sin \theta_f \\ 0 & 1 & 0 \\ -\sin \theta_f & 0 & \cos \theta_f \end{pmatrix} \quad (22)$$

$$\Theta_w(x, y) = \begin{pmatrix} l_1 & m_1 & n_1 \\ l_2 & m_2 & n_2 \\ l_3 & m_3 & n_3 \end{pmatrix} = \begin{pmatrix} 0 & \cos \theta_w & \sin \theta_w \\ -1 & 0 & 0 \\ 0 & -\sin \theta_w & \cos \theta_w \end{pmatrix} \quad (23)$$

where  $l_i, m_i, n_i$  ( $i = 1 \dots 3$ ) are the direction cosines between the RUC and material coordinate systems, and  $\theta_f, \theta_w$ , are the local undulation angles of fill and warp tows.

Based on (22), (23) the fill/warp stress rotation matrices are calculated as

$$T_q(x, y) = \begin{pmatrix} l_1^2 & m_1^2 & n_1^2 & 2m_1 n_1 & 2l_1 n_1 & 2l_1 m_1 \\ l_2^2 & m_2^2 & n_2^2 & 2m_2 n_2 & 2l_2 n_2 & 2l_2 m_2 \\ l_3^2 & m_3^2 & n_3^2 & 2m_3 n_3 & 2l_3 n_3 & 2l_3 m_3 \\ l_2 l_3 & m_2 m_3 & n_2 n_3 & m_2 n_3 + n_2 m_3 & l_2 n_3 + n_2 l_3 & l_2 m_3 + m_2 l_3 \\ l_1 l_3 & m_1 m_3 & n_1 n_3 & m_1 n_3 + n_1 m_3 & l_1 n_3 + n_1 l_3 & l_1 m_3 + m_1 l_3 \\ l_1 l_2 & m_1 m_2 & n_1 n_2 & m_1 n_2 + n_1 m_2 & l_1 n_2 + n_1 l_2 & l_1 m_2 + m_1 l_2 \end{pmatrix} \quad (24)$$

Performing the calculations indicated in (24) for the fill and warp yields

$$T_f(x, y) = \begin{bmatrix} c_f^2 & 0 & s_f^2 & 0 & 2c_f s_f & 0 \\ 0 & 1 & 0 & 0 & 0 & 0 \\ s_f^2 & 0 & c_f^2 & 0 & -2c_f s_f & 0 \\ 0 & 0 & 0 & c_f & 0 & -s_f \\ -c_f s_f & 0 & c_f s_f & 0 & c_f^2 - s_f^2 & 0 \\ 0 & 0 & 0 & s_f & 0 & c_f \end{bmatrix} \quad (25)$$

$$T_w(x, y) = \begin{bmatrix} 0 & c_w^2 & s_w^2 & 2c_w s_w & 0 & 0 \\ 1 & 0 & 0 & 0 & 0 & 0 \\ 0 & s_w^2 & c_w^2 & -2c_w s_w & 0 & 0 \\ 0 & 0 & 0 & 0 & -c_w & s_w \\ 0 & -c_w s_w & c_w s_w & c_w^2 - s_w^2 & 0 & 0 \\ 0 & 0 & 0 & 0 & -s_w & -c_w \end{bmatrix} \quad (26)$$

where  $s = \sin \theta(x, y)$  and  $c = \cos \theta(x, y)$ . Based on (21) and (25), (26), the transformed fill and warp 3D compliance matrices in global  $(x, y, z)$  c.s., at any  $(x, y)$  location of the RUC, are

$$\begin{aligned}\bar{S}_f(x, y) &= (T_f(x, y))^T \cdot S \cdot T_f(x, y) \\ \bar{S}_w(x, y) &= (T_w(x, y))^T \cdot S \cdot T_w(x, y)\end{aligned}\quad (27)$$

which after performing the calculations become

$$\begin{aligned}\bar{S}_f(x, y) &= \begin{bmatrix} S_{11} & S_{12} & S_{13} & 0 & S_{15} & 0 \\ S_{21} & S_{22} & S_{23} & 0 & S_{25} & 0 \\ S_{31} & S_{32} & S_{33} & 0 & S_{35} & 0 \\ 0 & 0 & 0 & S_{44} & 0 & S_{46} \\ S_{51} & S_{52} & S_{53} & 0 & S_{55} & 0 \\ 0 & 0 & 0 & S_{64} & 0 & S_{66} \end{bmatrix}_f (x, y) \\ \bar{S}_w(x, y) &= \begin{bmatrix} S_{11} & S_{12} & S_{13} & S_{14} & 0 & 0 \\ S_{21} & S_{22} & S_{23} & S_{24} & 0 & 0 \\ S_{31} & S_{32} & S_{33} & S_{34} & 0 & 0 \\ S_{41} & S_{42} & S_{43} & S_{44} & 0 & 0 \\ 0 & 0 & 0 & 0 & S_{55} & S_{56} \\ 0 & 0 & 0 & 0 & S_{65} & S_{66} \end{bmatrix}_w (x, y)\end{aligned}\quad (28)$$

By considering the plane-stress assumption in the  $(x, y)$  plane of the laminate, the reduced stiffness matrices of the fill and warp constituents, at any  $(x, y)$  location of the RUC, are calculated as

$$\bar{Q}_q(x, y) = \begin{bmatrix} \bar{Q}_{11} & \bar{Q}_{12} & 0 \\ \bar{Q}_{21} & \bar{Q}_{22} & 0 \\ 0 & 0 & \bar{Q}_{66} \end{bmatrix}_q = \begin{bmatrix} \bar{S}_{11} & \bar{S}_{12} & 0 \\ \bar{S}_{21} & \bar{S}_{22} & 0 \\ 0 & 0 & \bar{S}_{66} \end{bmatrix}_q^{-1}\quad (29)$$

where  $q = f, w$  indicates fill and warp, respectively, and the required  $\bar{S}_{ij}$  ( $i, j = 1, 2, 6$ ) terms in (29) are taken from the corresponding terms in (28).

From the configuration of the compliance matrices in (28) it can be seen that, due to 3D undulated configuration of the fill and warp tows, out of plane compliance terms exist (i.e., any term with subscript indices different from 1, 2, 6). The out of plane compliance terms induce out of plane coupling stress-strain components in the fill/warp constituents under in-plane loading. The above plane-stress assumption implies dropping the out of plane coupling terms, which has to be recorded as a simplification of the analytical model.

A similar approach based on the theory of UD ply can be applied for the calculation of the hygro-thermal properties of individual fill/warp tows. Thus, the 3D vectors of thermal and moisture expansion coefficients at any  $(x, y)$  location inside RUC are

$$\begin{Bmatrix} \alpha_x \\ \alpha_y \\ \alpha_z \\ \frac{1}{2}\alpha_{yz} \\ \frac{1}{2}\alpha_{xz} \\ \frac{1}{2}\alpha_{xy} \end{Bmatrix}_q (x, y) = [T]_q^{-1}(x, y) \cdot \begin{Bmatrix} \alpha_1 \\ \alpha_2 \\ \alpha_3 \\ 0 \\ 0 \\ 0 \end{Bmatrix}_q\quad (30)$$

$$\begin{Bmatrix} \beta_x \\ \beta_y \\ \beta_z \\ \frac{1}{2}\beta_{yz} \\ \frac{1}{2}\beta_{xz} \\ \frac{1}{2}\beta_{xy} \end{Bmatrix}_q (x, y) = [T]_q^{-1}(x, y) \cdot \begin{Bmatrix} \beta_1 \\ \beta_2 \\ \beta_3 \\ 0 \\ 0 \\ 0 \end{Bmatrix}_q\quad (31)$$

where  $\alpha_i, \beta_i$  ( $i = 1 \dots 3$ ) are the thermal and moisture expansion coefficients of the tow regarded as UD composite at tow fiber volume fraction  $V_t^f$  (see Section 2.1), calculated based on micro-mechanical models [2, 37–39]. The in-plane terms of interest are calculated as

$$\begin{aligned}
 \alpha_x^f(x, y) &= \alpha_1 c_f^2 + \alpha_2 s_f^2 & \alpha_y^f(x, y) &= \alpha_2 & \alpha_{xy}^f(x, y) &= 0 \\
 \alpha_x^w(x, y) &= \alpha_2 & \alpha_y^w(x, y) &= \alpha_1 c_w^2 + \alpha_2 s_w^2 & \alpha_{xy}^w(x, y) &= 0 \\
 \beta_x^f(x, y) &= \beta_1 c_f^2 + \beta_2 s_f^2 & \beta_y^f(x, y) &= \beta_2 & \beta_{xy}^f(x, y) &= 0 \\
 \beta_x^w(x, y) &= \beta_2 & \beta_y^w(x, y) &= \beta_1 c_w^2 + \beta_2 s_w^2 & \beta_{xy}^w(x, y) &= 0
 \end{aligned} \tag{32}$$

## References

- [1] B.N. Cox. Handbook of analytical methods for textile composites. Technical Report NASA Contractor Report 4750, NASA Langley Research Center, March 1997.
- [2] E. J. Barbero. *Introduction to Composite Materials Design - Second Edition*. CRC, Boca Raton, FL, 2010.
- [3] T. Ishikawa, M. Matsushima, Y. Hayashi, and T. W Chou. Experimental confirmation of the theory of elastic moduli of fabric composites. *Journal of Composite Materials*, 19(5):443–58, 1985.
- [4] Ajit K. Roy. In situ damage observation and failure in model laminates containing planar yarn crimping of woven composites. *Mechanics of composite materials and structures*, 3(2):101–117, 1996.
- [5] N. Naik and V. Ganesh. Thermo-mechanical behavior of plain weave fabric composites: Experimental investigations. *J Materials Sci*, 32:267–277, 1997.
- [6] T. Ishikawa and T. W. Chou. Stiffness and strength behavior of woven fabric composites. 71:3211–3220, 1982.
- [7] T-W. Chou. *Microstructural Design of Fiber Composites*. Cambridge University Press, Cambridge, MA., 1992.
- [8] T. Ishikawa and Tsu-Wei Chou. Elastic behavior of woven hybrid composites. *Journal of Composite Materials*, 16:2–19, 1982.
- [9] M. Ito and T-W. Chou. Elastic moduli and stress field of plain weave composites under tensile loading. *Compos Sci Technol*, 57:787–800, 1997.
- [10] M. Ito and T-W. Chou. An analytical and experimental study of strength and failure behavior of plain weave composites. *J Compos Mater*, 32(1):2–30, 1998.
- [11] A. Adumitroaie and E. J. Barbero. Stiffness and strength prediction for plain weave textile reinforced composites. *Mechanics of Advanced Materials and Structures*, xx(xx):xx, 2010.
- [12] N. Naik and V. Ganesh. Prediction of on-axis elastic properties of plain weave fabric composites. *Compos Sci Technol*, 45:135–152, 1992.
- [13] N. Naik. *Woven Fabric Composites*. Technomic, Lancaster, PA, 1994.
- [14] N. K. Naik and V. K. Ganesh. Analytical method for plain weave fabric composites. *Composites*, 26(4):281–289, 1995.
- [15] N. Naik and V. Ganesh. Failure behavior of plain weave fabric laminates under on-axis uniaxial tensile loading: I - Laminate geometry. *J Compos Mater*, 30(16):1748–1778, 1996.
- [16] N. Naik and V. Ganesh. Failure behavior of plain weave fabric laminates under on-axis uniaxial tensile loading: II - Analytical predictions. *J Compos Mater*, 30(16):1779–1882, 1996.
- [17] N. Naik and V. Ganesh. Failure behavior of plain weave fabric laminates under on-axis uniaxial tensile loading: III - Effect of fabric geometry. *J Compos Mater*, 30(16):1883–1856, 1996.
- [18] R. A. Naik. Analysis of woven and braided fabric reinforced composites. Technical Report NASA Contractor Report 194930, June 1994.
- [19] R. A. Naik. Failure analysis of woven and braided fabric reinforced composites. *Journal of Composite Materials*, 29(17):2334–63, 1995.
- [20] D. Scida and Z. Aboura. Prediction of the elastic behavior of hybrid and non-hybrid woven composites. *Compos Sci Technol*, 59:1727–1740, 1997.

- [21] D. Scida and Z. Aboura. A micromechanics model for 3D elasticity and failure of woven fiber composite materials. *Compos Sci Technol*, 59:505–517, 1999.
- [22] J. Falzon and I. Herszberg. Effects of compaction on the stiffness and strength of plain weave fabric RTM composites. *J Compos Mater*, 30(11):1210–1247, 1996.
- [23] I. S. Raju and J. T. Wang. Classical laminate theory models for woven fabric composites. *Journal of Composites Technology and Research*, 16(4):289–303, 1994.
- [24] Zheng-Ming Huang and S. Ramakrishna. Towards automatic designing of 2D biaxial woven and braided fabric reinforced composites. *Journal of Composite Materials*, 36(13):1541–79, 2002.
- [25] Zheng-Ming Huang. Efficient approach to the structure-property relationship of woven and braided fabric-reinforced composites up to failure. *Journal of Reinforced Plastics and Composites*, 24(12):1289–1309, 2005.
- [26] Zheng-Ming Huang. Simulation of the mechanical properties of fibrous composites by the bridging micromechanics model. *Composites Part A*, 32(2):143–172, 2001.
- [27] S. Z. Sheng and S. V. Hoa. Three dimensional micro-mechanical modeling of woven fabric composites. *J Compos Mater*, 35:1701–1729, 2001.
- [28] E. J. Barbero, J. Trovillion, J.A. Mayugo, and K.K. Sikkil. Finite element modeling of plain weave fabrics from photomicrograph measurements. *Composite Struct*, 73(1):41–52, 2006.
- [29] V. R. Aitharaju and R. C. Averill. Three-dimensional properties of woven-fabric composites. *Composites Science and Technology*, 59(12):1901–11, 1999.
- [30] D. M. Blacketter, D. E. Walrath, and A. C. Hansen. Modeling damage in a plain weave fabric-reinforced composite material. *Journal of Composites Technology and Research*, 15(2):136–42, 1993.
- [31] Xiaodong Tang and John D. Whitcomb. Progressive failure behaviors of 2d woven composites. *Journal of Composite Materials*, 37(14):1239–1259, 2003.
- [32] E. J. Barbero, P. Lonetti, and K. Sikkil. Finite element continuum damage modeling of plain weave reinforced composites. *Composites” part B*, 37:137–147, 2006.
- [33] A. Adumitroaie and E. J. Barbero. Modeling of woven fabric reinforced composites - I. geometrical model. *xxx, xx(xx):xx, 20xx*.
- [34] ASTM International. ASTM D2584 Standard Test Method for Ignition Loss of Cured Reinforced Resins, vol. 08.01.
- [35] ASTM International. ASTM D3171 Standard Test Methods for Constituent Content of Composite Materials, vol. 15.03.
- [36] P. Vandeurzen, J. Ivens, and I. Verpoest. A three-dimensional micromechanical analysis of woven-fabric composites. II. Elastic analysis. *Composites Science and Technology*, 56(11):1317–27, 1996.
- [37] E. J. Barbero. *Finite Element Analysis of Composite Materials*. CRC Press, Boca Raton, FL, 2007.
- [38] K. K. Stellbrink. *Micromechanics of Composites*. Hanser Publishers, Munich, 1996.
- [39] J. W. Weeton, D. M. Peters, and K. L. Thomas, editors. *Engineer’s Guide to Composite Materials*. ASM Int, OH, 1986.
- [40] E. J. Barbero. Web resource: <http://www.mae.wvu.edu/barbero/cadec.html>.
- [41] R. Luciano and E. J. Barbero. Formulas for the stiffness of composites with periodic microstructure. *Int J Solids Struct*, 31(21):2933–2944, 1994.